Geology of the Gusev cratered plains from the Spirit rover transverse

M. P. Golombek,[1] L. S. Crumpler,[2] J. A. Grant,[3] R. Greeley,[4] N. A. Cabrol,[5] T. J. Parker,[1] J. W. Rice Jr.,[4] J. G. Ward,[6] R. E. Arvidson,[6] J. E. Moersch,[7] R. L. Fergason,[4] P. R. Christensen,[4] A. Castaño,[1] R. Castaño,[1] A. F. C. Haldemann,[1] R. Li,[8] J. F. Bell III,[9] and S. W. Squyres[9]

[1] The cratered plains of Gusev traversed by Spirit are generally low-relief rocky plains dominated by impact and eolian processes. Ubiquitous shallow, soil-filled, circular depressions, called hollows, are modified impact craters. Rocks are dark, fine-grained basalts, and the upper 10 m of the cratered plains appears to be an impact-generated regolith developed over intact basalt flows. Systematic field observations across the cratered plains identified vesicular clasts and rare scoria similar to original lava flow tops, consistent with an upper inflated surface of lava flows with adjacent collapse depressions. Crater and hollow morphometry are consistent with most being secondaries. The size-frequency distribution of rocks >0.1 m diameter generally follows exponential functions similar to other landing sites for total rock abundances of 5–35%. Systematic clast counts show that areas with higher rock abundance and more large rocks have higher thermal inertia. Plains with lower thermal inertia have fewer rocks and substantially more pebbles that are well sorted and evenly spaced, similar to a desert pavement or lag. Eolian bed forms (ripples and wind tails) have coarse surface lags, and many are dust covered and thus likely inactive. Deflation of the surface ~5–25 cm likely exposed two-toned rocks and elevated ventifacts and transported fines into craters creating the hollows. This observed redistribution yields extremely slow average erosion rates of ~0.03 nm/yr and argues for very little long-term net change of the surface and a dry and desiccating environment similar to today's since the Hesperian (or ~3 Ga).

1. Introduction

[2] Gusev crater was selected as the landing site for the Spirit rover based on its morphology, which suggests a lake occupied the crater as a result of water and sediment discharge from the 800-km-long channel Ma'adim Vallis that drained through the highlands and breached the southern rim. Prior to landing, based dominantly on 250 m/pixel to 72 m/pixel regional Viking orbiter images, the plains within Gusev were mostly viewed as the remnants of material deposited from Ma'adim Vallis during prolonged fluvial, lacustrine and possibly glacial episodes [e.g., *Carr and Clow*, 1981; *Brakenridge*, 1990; *Goldspiel and Squyres*, 1991; *Cabrol et al.*, 1998; *Grin and Cabrol*, 1997; *Kuzmin et al.*, 2000; *Irwin et al.*, 2002].

[3] The age and timing of events in the putative fluvio-lacustrine system were investigated using impact crater counts and geologic mapping. *Greeley and Guest* [1987] observed that the Ma'adim drainage system dissected Noachian cratered highland material [*Tanaka*, 1986]. *Kuzmin et al.* [2000] showed Gusev is an Early to Middle Noachian crater, with aqueous sedimentation and ponding beginning in the Late Noachian from small valley networks on the eastern and southern portion of the crater rim. Ma'adim Vallis formed during the Early Hesperian with possible fluvio-lacustrine activity continuing discontinuously throughout the Hesperian. Early Amazonian possible glacial activity was suggested from observations of tongue-like lobe morphologies with sinuous margins [*Kuzmin et al.*, 2000; *Cabrol et al.*, 1996].

[4] The advent of Mars Global Surveyor (MGS) and Mars Odyssey Thermal Emission Imaging System (THEMIS) imagery has refined interpretations of the geologic develop-

[1]Jet Propulsion Laboratory, California Institute of Technology, Pasadena, California, USA.

[2]New Mexico Museum of Natural History and Science, Albuquerque, New Mexico, USA.

[3]Smithsonian Institution, Washington, DC, USA.

[4]Department of Geological Sciences, Arizona State University, Tempe, Arizona, USA.

[5]NASA Ames Research Center, Moffett Field, California, USA.

[6]Department of Earth and Planetary Sciences, Washington University, St. Louis, Missouri, USA.

[7]Department of Geological Sciences, University of Tennessee, Knoxville, Tennessee, USA.

[8]Department of Civil and Environmental Engineering and Geodetic Science, Ohio State University, Columbus, Ohio, USA.

[9]Department of Astronomy, Cornell University, Ithaca, New York, USA.

ment of the Gusev crater interior (Figure 1) [*Christensen et al.*, 2005; *Martínez-Alonso et al.*, 2005]. The surface upon which the majority of the landing ellipse was sited [*Golombek et al.*, 2003a], appears as a cratered plain in Mars Orbiter Camera (MOC) images, lacking obvious diagnostic morphologies to indicate a particular origin. THEMIS images, however, show what appears to be a young, 150 km-long viscous flow emanating from the mouth of Ma'adim Vallis and terminating near the northern limit of the crater floor (Figure 1) [*Rice et al.*, 2003]. This flow has a rumpled surface texture with longitudinal ridges. It overlies the cratered plains and covers the western half of the landing ellipse. The thermal properties of the flow in THEMIS Infrared (IR) images are indistinct relative to those of the surrounding plains, indicating either that it is mantled with dust that is at

least a few cm thick [*Rice et al.*, 2003], or that its surface properties are similar to the plains materials on the adjacent Gusev interior floor.

[5] The fact that the flow with longitudinal ridges and elevated lobate margins can be traced back up Ma'adim Vallis all the way to the source regions of the channel, several hundred kilometers south of Gusev suggests it is fluvial. The lack of obvious fluvial morphologies argues that the flow in Gusev crater is a debris flow with 15–40% water by volume [*Allen*, 1985], as hyperconcentrated flows (40–80% water by volume) would be turbulent rather than laminar [*Komar*, 1979] and would be expected to form familiar fluvial scour and depositional morphologies, such as streamlined islands and longitudinal ridge and groove structures parallel to the flow direction. Windows through
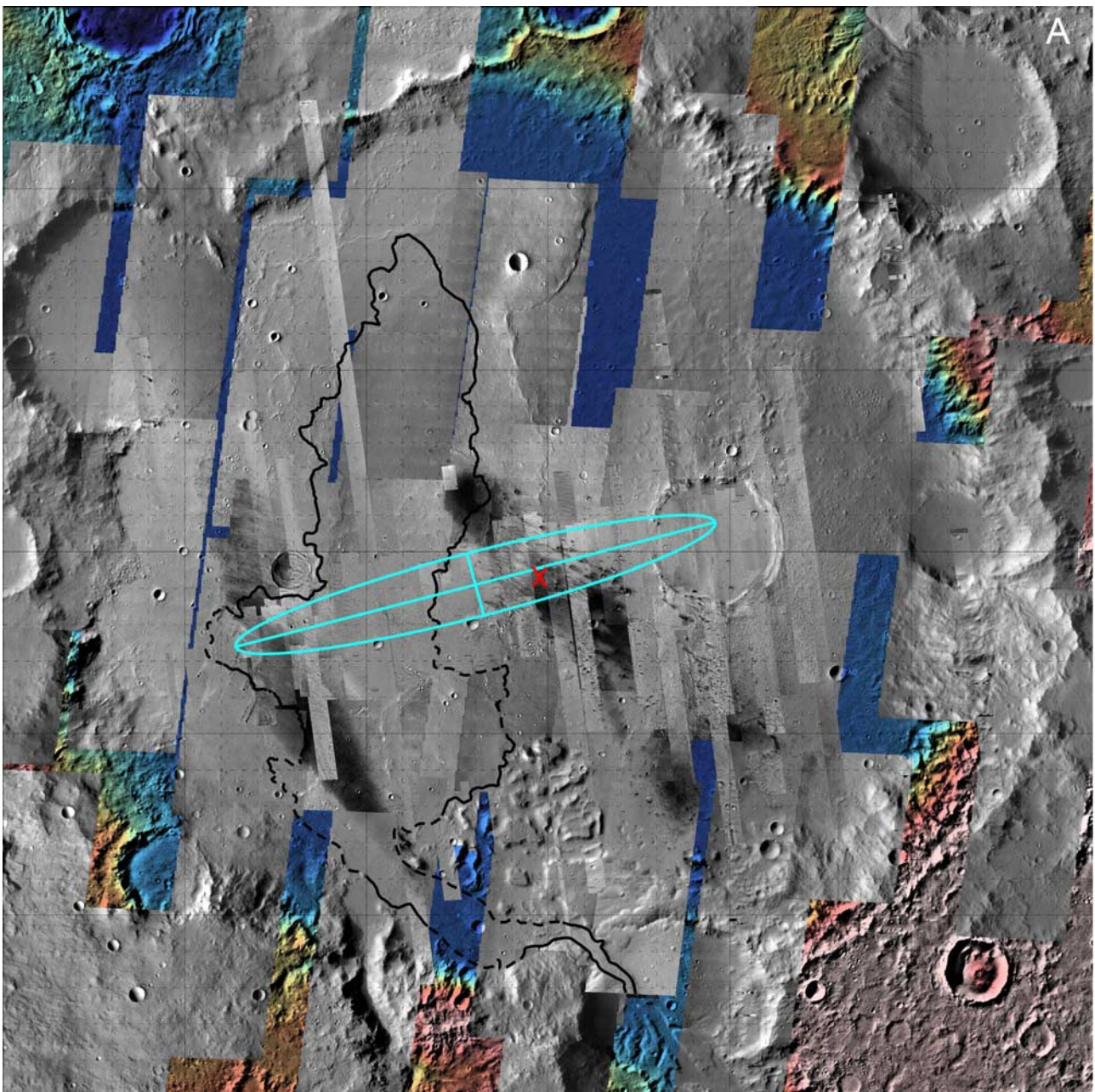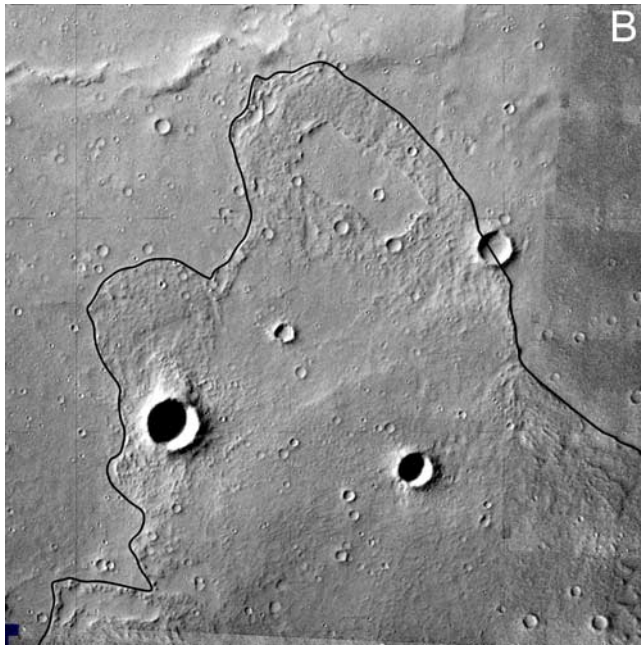

Figure 1

Figure 1. (continued)

the flow to the plains beneath are also found, the most prominent of which is shown in Figure 1b near its terminus. The 4 km wide rectilinear window is surrounded by pressure ridges that might be explained by a large ice raft that was entrained by the debris flow but has since sublimated, although other interpretations of the flow and window are possible (Figure 1b).

[6] Other possible origins of the floor material in Gusev were considered via the interpretation of MOC images prior to landing including volcanic material originating from Apollinaris Patera (e.g., air falls, tuffs, pyroclasts); volcanic flows derived from within Gusev; ejecta deposits from regional impacts; glacial deposits and subsurface hydrothermal processes; as well as globally derived atmospheric dust deposits and coarser-grained wind-deposited material derived from local and regional sources [*McCauley*, 1973], which became dominant after the Middle Amazonian. Sur-

face observations to test each of these hypotheses using the Spirit rover were discussed by *Golombek et al.* [2003a] and *Cabrol et al.* [2003].

[7] Although not favored by a majority of investigators prior to landing, a volcanic origin for the plains in Gusev was considered. The closest, most noticeable volcanic construct in the Aeolis region is Apollinaris Patera, a large shield volcano, located 300 km north of Gusev. A second possible volcanic construct, Aeolis [*Hodges and Moore*, 1994], lies 300 km to the south-southwest. However, no obvious lava flows can be traced from Apollinarus Patera or Aeolis into Gusev. Numerous wrinkle ridges are located on the floor of Gusev crater implying that the plains could be primarily volcanic [*Greeley et al.*, 2005a; *Rice et al.*, 2003], based on the analogy with wrinkle ridges on the lunar basaltic mare and recent work that indicates wrinkle ridges are fault-propagation folds in which motion on blind thrust faults at depth is accommodated by interlayer slip and folding in strong surface layers (e.g., basalts) [*Mueller and Golombek*, 2004]. Thermal Emission Spectrometer (TES) and THEMIS spectra obtained from orbit before landing implied that the floor of Gusev was covered with dust and olivine basalt (S. Ruff, personal communication, 2005). The source of the lava flows that cover most of the floor of Gusev may have been from fissure style eruptions, which have been either buried or otherwise obscured.

[8] This paper provides an overview of the geology of the Gusev cratered plains as observed by Spirit during her traverse [*Arvidson et al.*, 2006]. The paper builds on the science results and observations reported after the nominal mission [*Squyres et al.*, 2004; *Arvidson et al.*, 2004; *Bell et al.*, 2004; *Christensen et al.*, 2004a; *Grant et al.*, 2004; *Greeley et al.*, 2004; *Herkenhoff et al.*, 2004; *Lemmon et al.*, 2004; *McSween et al.*, 2004]. It summarizes work on similar topics that appear in more detail in other papers that have been published or are in this volume [*Crumpler et al.*, 2005; *Golombek et al.*, 2005a; *Grant et al.*, 2006; *Greeley et al.*, 2006; *Li et al.*, 2006; *Fergason et al.*, 2006; *Yen et al.*, 2005], but covers other topics more thoroughly that are not covered elsewhere. The paper begins with a description of the morphology of the plains from the surface and as mapped in high-resolution MOC images (section 2). Next,

Figure 1. Gusev crater mosaics showing final targeted landing ellipse, landing location, and outline of young flow emanating from the mouth of Ma'adim Vallis. (a) Mosaic shows regional context including Gusev crater, with Ma'adim Vallis breaching the wall and entering the crater from the south. Young flow emanating from Ma'adim Vallis that extends over 150 km is outlined. The blue ellipse is the final targeted ellipse, EP55A4 after launch in September 2003, centered at 14.59°S, 175.30°E and 78.25 km long by 10.41 km wide oriented at an azimuth of 75°, which differs slightly from the prelaunch ellipse EP55A3 shown by *Golombek et al.* [2003a], which is centered at 14.59°S, 175.30°E and is 81 km long by 12 km wide oriented at an azimuth of 75°. The red cross is the landing location. The background of the mosaic is the Viking MDIM 2.0 mosaic, overlaid by Mars Orbiter Laser Altimeter (MOLA) elevations in color. Thin image strips mostly oriented to the north-northwest are Mars Orbiter Camera (MOC) high-resolution images. Wider image strips mostly oriented to the north-northeast are Mars Odyssey Thermal Emission Imaging System (THEMIS) visible images at 18 m/pixel. The mosaic includes 13°−16°S latitude and 174°−177°E longitude in the MOLA IAU 2000 reference frame; solid black lines in Figures 1a and 1b are 0.5° (∼30 km), and the dashed black grid is 0.1° (∼6 km). (b) Detail of terminus of young flow showing rumpled texture, with 4-km-wide window near the terminus through the deposit into underlying plains. Because the flow can be traced up the Ma'adim Vallis channel, fluvial discharge likely transitioned from a hyperconcentrated to a debris flow as water was lost via infiltration, evaporation, and freezing, effectively raising the sediment load, increasing the viscosity, and damping the turbulence into a viscous laminar flow. Alternatively, the flow could be volcanic but would require a source region in the channel. The background is the THEMIS visible image mosaic, about 18 km wide.
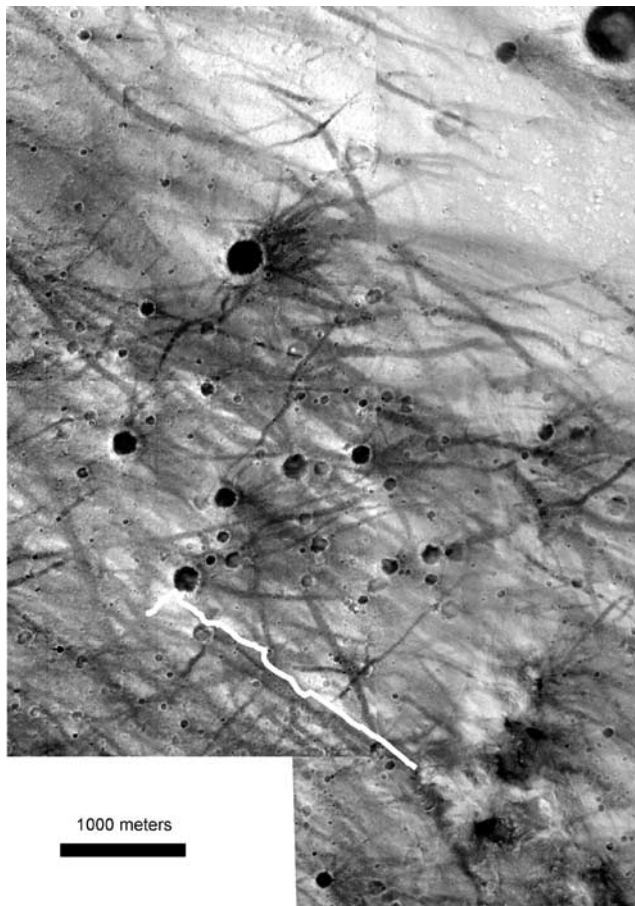
Figure 2. MOC images of Spirit landing and traverse area. The image shows cratered plains, with most crater interiors darker than the plains as well as dark dust devil tracks (darker from the removal of dust). Spirit landed southwest of Bonneville in a dark dust devil track, traversed to the southern rim of Bonneville crater, and then roved 2 km to the southeast to the Columbia Hills (traverse across the cratered plains shown in white). MOC images R07-01606 and R13-01467; north is up.

hollows (circular soil-filled depressions typically with rocky rims) are described and compared favorably to small impact craters observed from orbit (section 3). The 4 large craters visited by Spirit are described and the morphometry of craters and hollows discussed as a clue to their origin (section 4). The size frequency distributions of rocks, clasts and pebbles are discussed next (section 5) and eolian features are described (section 6). The surficial geology is summarized and a volcanic origin for the plains modified by impact and lesser eolian activity is concluded (section 7). Finally, the gradational history of the plains is described and constraints on the climate are derived from the rate of redistribution of sediment (section 8).

## 2. Morphology of the Cratered Plains

2.1. Introduction

[9] Spirit landed on the cratered plains unit of the Gusev crater floor, ~10 km east of the ellipse center [*Golombek et*

al., 2003a] in a region of low albedo, characterized by many dark streaks interpreted to be dust devil tracks (Figures 1 and 2). This resulted in substantially lower albedo and much less dust at the landing site, named the Columbia Memorial Station (CMS) than average for the ellipse and the Gusev area in general [*Golombek et al.*, 2003a]. In high-resolution MOC images (Figure 2), prior to landing, the plains were characterized by a large number of craters generally smaller than several hundred meters in diameter, many of which appeared degraded with scalloped rims and shallow flat floors [*Hurst et al.*, 2004; *McEwen et al.*, 2005]. This terrain (cratered plains) was evaluated to be the least hazardous of the terrains available for locating the ellipse based on landing simulations on MOC derived digital topography
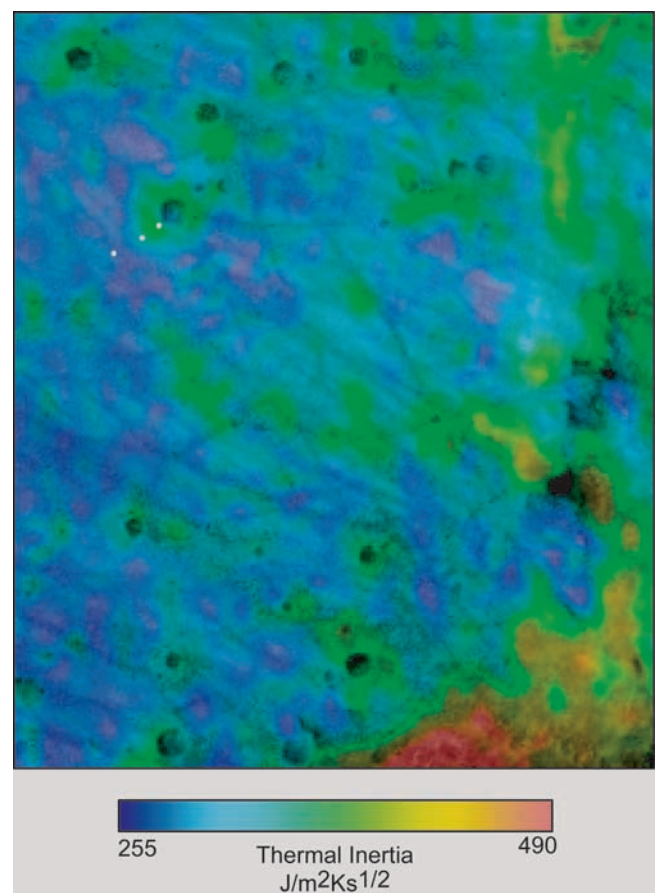
Figure 3. THEMIS thermal inertia image in color (100 m/pixel) overlaid on THEMIS visible images (18 m/pixel). Spirit landed at Columbia Memorial Station (CMS) in low-albedo, low-thermal-inertia intercrater plains (southwestern-most white dot, Mission Success panorama) and traversed through the ejecta blanket (Legacy panorama, middle white dot) to the rim of Bonneville crater about 300 m away (northeastern most white dot) and then across the low- and high-thermal-inertia plains to the Columbia Hills (with generally higher inertias) to the east and southeast. Thermal inertia [*Fergason and Christensen*, 2003] increases from 285 to 330 over the traverse to the rim of Bonneville crater, with rock size frequency distributions reported at these three locations.
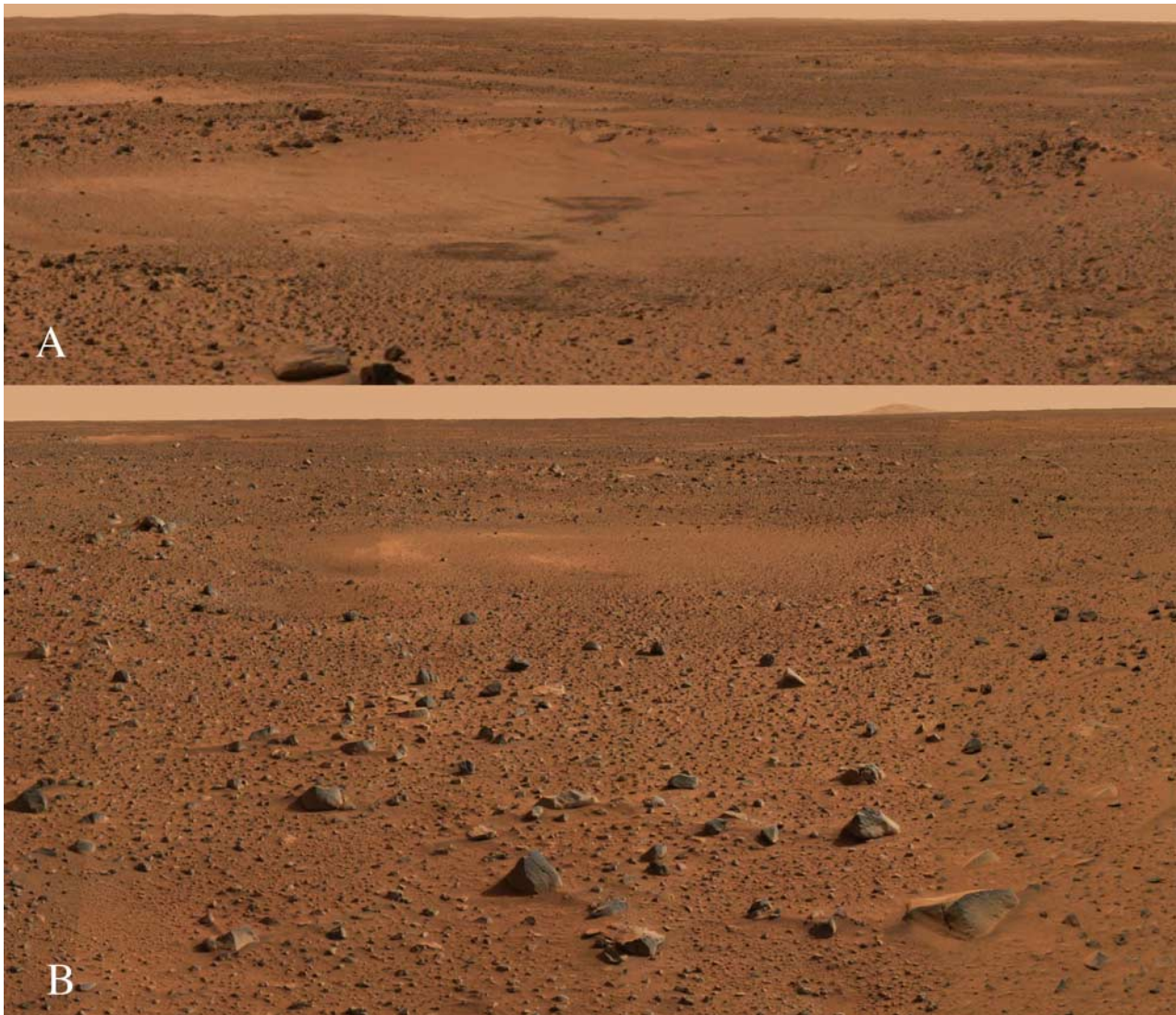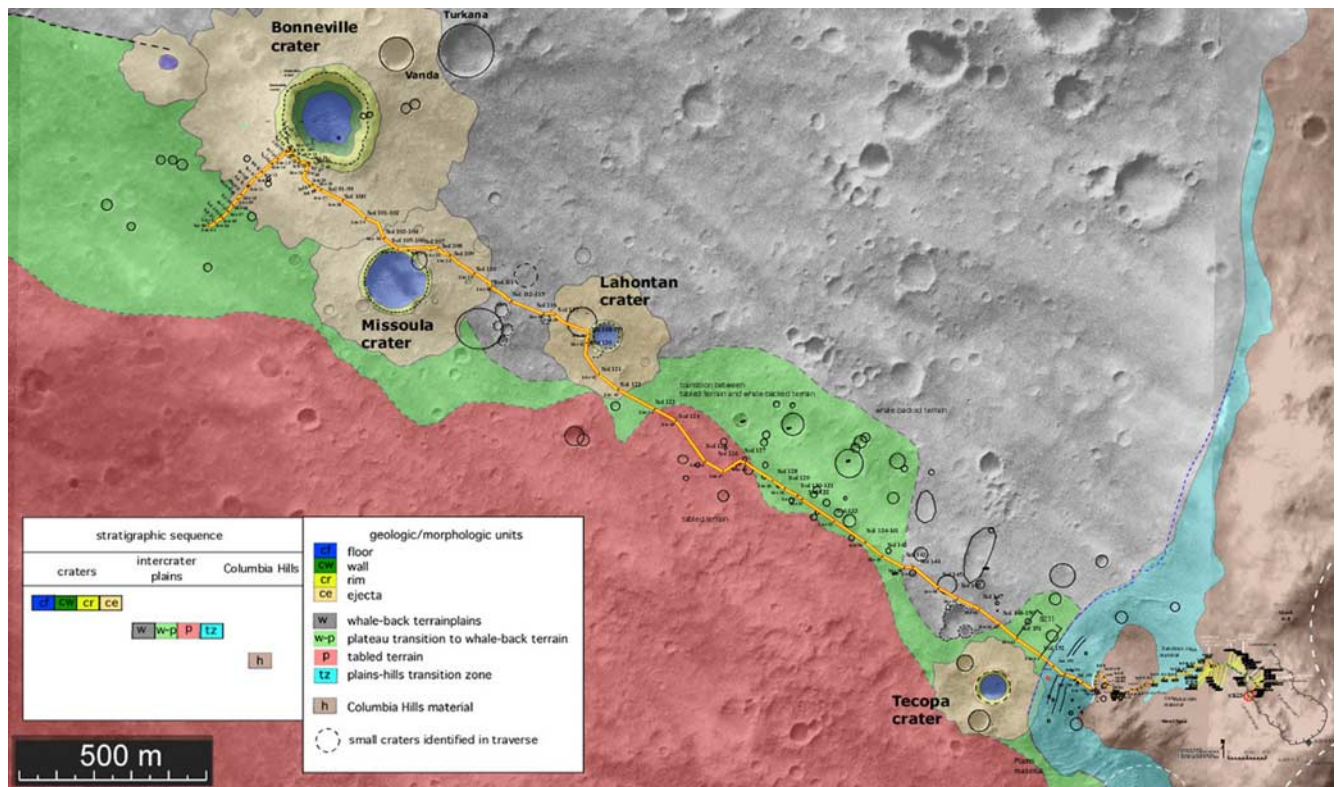
Figure 4. Portions of Mission Success panorama at Columbia Memorial Station. Mosaic (about $110°-170°$) shows sediment-filled hollows, "Sleepy" ($\sim$20 m diameter) in the foreground (Figure 4a) and "Drowsy" ($\sim$15 m diameter) (Figure 4b). (a) Note surface dust disturbed and made darker by airbag bounces and rocky rings at edge of hollows. (b) Mosaic (about $0°-60°$) shows angular, dark, fine-grained rocks, pebble-rich surface similar to a desert pavement, sediment-filled hollows, and Grissom Hill on horizon. Note dark drifts of eolian material (wind tails) to the left of dark rocks in left, middle foreground.

of the surface [*Kirk et al.*, 2003] sprinkled with rocks [*Golombek et al.*, 2003a]. The closest etched terrain of higher relief (and older age), judged to be more hazardous for landing [*Golombek et al.*, 2003a], is the Columbia Hills $\sim$2 km to the southeast.

[10] The THEMIS thermal inertia [*Fergason and Christensen*, 2003] of the plains (Figure 3) shows surfaces with different thermophysical properties. Crater rims and relatively fresh ejecta have high thermal inertia (>300 J/m^2 K s$^{0.5}$). Low-thermal-inertia intercrater plains have inertias of <290 J/m^2 K s$^{0.5}$. High-thermal-inertia plains have slightly higher thermal inertias in between those of the ejecta and low-inertia plains. As discussed later (section 5), the thermal inertia increases as the rock abundance increases [*Golombek et al.*, 2005a; *Moersch et al.*, 2005], although there is some evidence that the fine component thermal inertia also varies [*Golombek et al.*, 2005a].

[11] The landing site is a generally low-relief, somewhat rocky plain dominated by shallow circular depressions with rocky rims and smooth soil-filled centers called hollows (Figure 4). Low ridges in view from CMS include the Columbia Hills to the east ($\sim$100 m high) and the rim of Bonneville crater (200 m diameter) forms the horizon 240 m to the northeast. Boulder and cobbles are rare; the largest rock within 20 m of the lander is <0.5 m diameter [*Grant et al.*, 2004]; total rock coverage averages about 7%. A vast majority of the rocks appear dark, fine grained and pitted. Many appear to be ventifacts, with flutes and grooves formed by impacting sand in saltation [*Greeley et al.*, 2004]. Most rocks appear coated with dust and some lighter toned rocks have weathering rinds whose formation may have involved small amounts of water [*McSween et al.*, 2004]. The chemistry and mineralogy of the rocks described elsewhere (and the pits as vesicles) appear to be consistent

Figure 5. Plains traverse route and geologic/morphologic terrains units mapped from MOC image data. Units described in text. MOC images R15-02643 and R20-01024.

with olivine basalts [*McSween et al.*, 2004, 2006] and the soil appears to be mostly basaltic, similar to soil elsewhere on Mars [*Yen et al.*, 2005]. No outcrop of intact rocks or layers of rocks have been observed anywhere along Spirit's traverse of the cratered plains or the imaged interiors of 4 large craters (>100 m diameter) observed before entering the Columbia Hills.

[12] The traverse across the plains from CMS to Bonneville crater to the Columbia Hills enabled widespread, basic field geologic observations that provided substantial information into the potential origin of the plains over the transect (Figure 5). Two origins for the plains have been proposed to explain the Spirit observations: (1) debris sheets from the outflow of Ma'adim Vallis and (2) primary lava flows modified by impact and eolian processes [*Grant et al.*, 2004; *Squyres et al.*, 2004; *Greeley et al.*, 2004]. Although it cannot be entirely ruled out that the plains are fluvial debris of basaltic origin that have been reworked as suggested by the young viscous flow emanating from Ma'adim Vallis, overall the plains surface as viewed from Spirit bears few identifiable examples of fluvial morphologies such as rounded boulders, channels, local scouring, or interbedded fines and clasts. A simple comparison with the Mars Pathfinder landing site, which has streamlined hills, tabular subrounded and rounded boulders, imbricated rocks, and likely drainage troughs that were produced by catastrophic floods [*Golombek et al.*, 1997] underscores this difference. Most of the characteristics of the Gusev cratered plains are consistent with modification of primary basaltic lava flow surfaces, including the presence of angular vesicular clasts, rocks with vesicular layers, delicate scoriaceous clasts, and

large blocks of basalt excavated from the larger impact craters.

[13] Craters are widely distributed throughout the plains, yet the surface is not saturated (see section 3). Therefore much of the relief at meters to tens of meters scale may be inherited from initial relief on the original surfaces. Tracking of the general character of the surface and rocks along the intercrater plains (sols 111–156) in relation to MOC image characteristics suggests that there are differences in the character of the surface and the local relief that are unrelated to impact craters.

2.2. Lithologic Variations

[14] The morphology of rocks varied along the traverse, but small vesicular clasts and angular and larger rocks that are generally less vesicular are most common. The abundance of each morphological type is in general uniform throughout the traverse, although an area of anomalous concentrations of vesicular clasts occurred between sols 110 and sol 111. This zone includes delicately spined scoria fragments (Potrillo and Yugama) up to 20 cm across and occurred after Spirit traversed from Missoula ejecta to the low-thermal-inertia intercrater plains, suggesting this unusual concentration was a preserved remnant of the original lava flow surface.

[15] Clues to the internal structure and alteration state of the plains lavas occur in the rims of the larger impact craters. Unusually altered–appearing clasts, including spheroidally weathered and case-hardened morphologies [*Crumpler et al.*, 2005] occurred only in the ejecta at or near the rims of Missoula and Bonneville crater, as did the
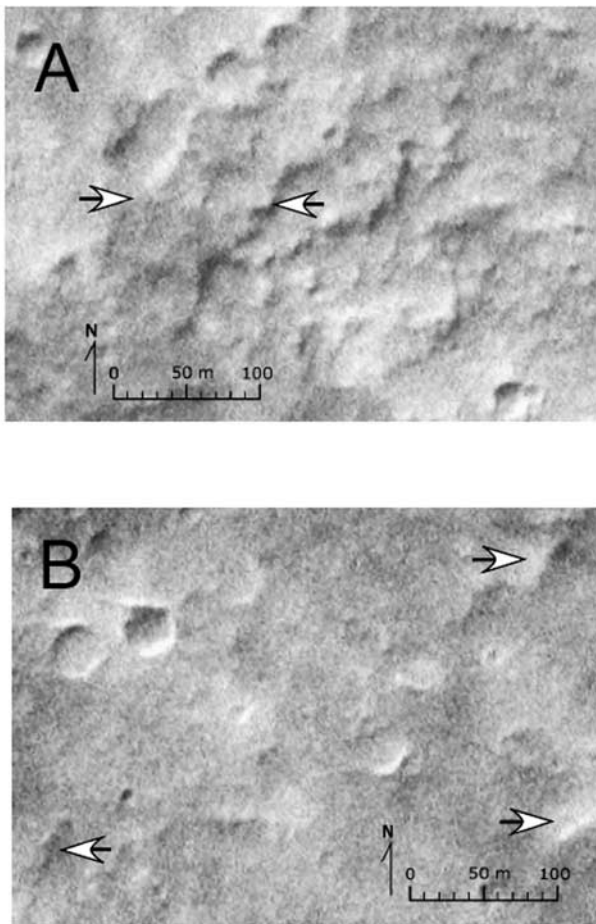
Figure 6. Reference areas for (a) "tabled terrain" and (b) "whale-backed terrain" from MOC images (examples denoted). MOC images R15-02643 and R20-01024.

largest (>1 m) rocks. These basic observations suggest that (1) the larger blocks result from deeper excavation of the plains basalt surface associated with larger impacts, and that these blocks show that the deeper interior consists of more massive materials with widely spaced fractures similar to dense lava flow interiors common to terrestrial basaltic lava flows and (2) the more altered lithologies may also be associated with the deeper interior of the plains basalts [Crumpler et al., 2005], suggesting that fluid residence in the deep interior was sufficiently long that chemical alteration of the basaltic lavas occurred.

2.3. Surface Map Units

[16] Morphologic mapping reveals differences in surface texture in MOC images from south to north (Figure 5). The orientation of the traverse route is approximately at a right angle to the apparent gradient from rough terrain characterized by local elongate plateaus or tables ("tabled terrain") to the south and widely dispersed hummocks or whale-back-shaped swells ("whale-backed terrain") to the north (Figure 6). The region to the south of the traverse appears rougher, and although there are numerous arcuate ridges suggestive of degraded rims of small impact craters, many of the swells are elongate in a roughly northeast-southwest orientation and are not obviously segments of small impact

crater rims. Northward of the traverse, the surface is defined by elongate swells, and farther northward the intensity of small craters is such that these small swells are lost in the clutter of impact crater-induced local relief. Lying between these two terrains is a transitional surface where whale-backs are somewhat more common, but tables are generally absent. THEMIS thermal inertia data correlate broadly with these apparent morphological units (Figure 3). High-thermal-inertia surfaces that are not obviously related to local impact craters constitute a significant fraction of the surface area south of the traverse in the tabled terrain. The proposed units also can be related to regional relief variations and detailed differences in surface character at rover scales.

[17] Most of the traverse eastward of the distal edges of the ejecta from Missoula crater crosses a low region of the whale-backed terrain. Following Lahontan crater (sols 126–140), the traverse ascends onto a surface within the tabled terrain. After sol 140, the traverse crosses the whale-backed terrain in an area where it is largely devoid of swells. At sol 151 the traverse ascends onto a blocky surface that in MOC images appears to be a north-northeast trending rise or lobe of the tabled terrain that abuts the Columbia Hills (reached on sol 156).

2.4. Plains Topographic Characteristics

[18] A regional south to north gradient between 0.4°–3.4° is detectable in the southeastward directed Navcam panoramas based on the departure of the near horizon from level; the southeast to south horizon is both closer and generally above level, suggesting the regional surface either grades upward to the south or that there is a ridge or escarpment to the south (Figure 7). In contrast, the northeast to east horizon generally falls below level. If the plains surface is a basaltic lava flow, these characteristics are consistent with a lava flow surface that was emplaced from a generally southward direction that flowed north-northeast with a surface gradient of at least 0.4°. The present surface gradient in Mars Orbiter Laser Altimeter (MOLA) topographic maps [Golombek et al., 2003a] of the plains traversed is also shallowly down to the north-northeast.

[19] The apparent relief characteristics (including swells), the regional gradient in the surface toward the north, and distinctions in the general morphology of rocks detectable in panoramic images can be compared with relief and surface elevation derived from rover tracking data. The surface elevation along the traverse from the landing site to the base of the Columbia Hills ascended approximately 20 m from west to east (a regional slope of 0.68°) (Figure 8a) [Li et al., 2006]. Superimposed on this general gradient are local variations of up to 9 m, which become more apparent when the relief is detrended along the traverse (Figure 8b). On the basis of the detrended relief data, the surface ascended along a gradient of approximately 0.9° from sol 120 to sol 126 (in addition to the regional gradient). Thereafter the surface descends until sol 128 along a gradient of 0.8° to a broad plateau that slopes more gently 0.3° to sol 142. From sol 142 to sol 146 the surface descends further along a gradient of 1.3° to sol 151 before ascending again along a gradient of 1° to the surface of a blocky swell that grades at about 0.3° to the base of the Columbia Hills.

[20] The observed variations in relief and slope across the plains from localization data can be compared with the
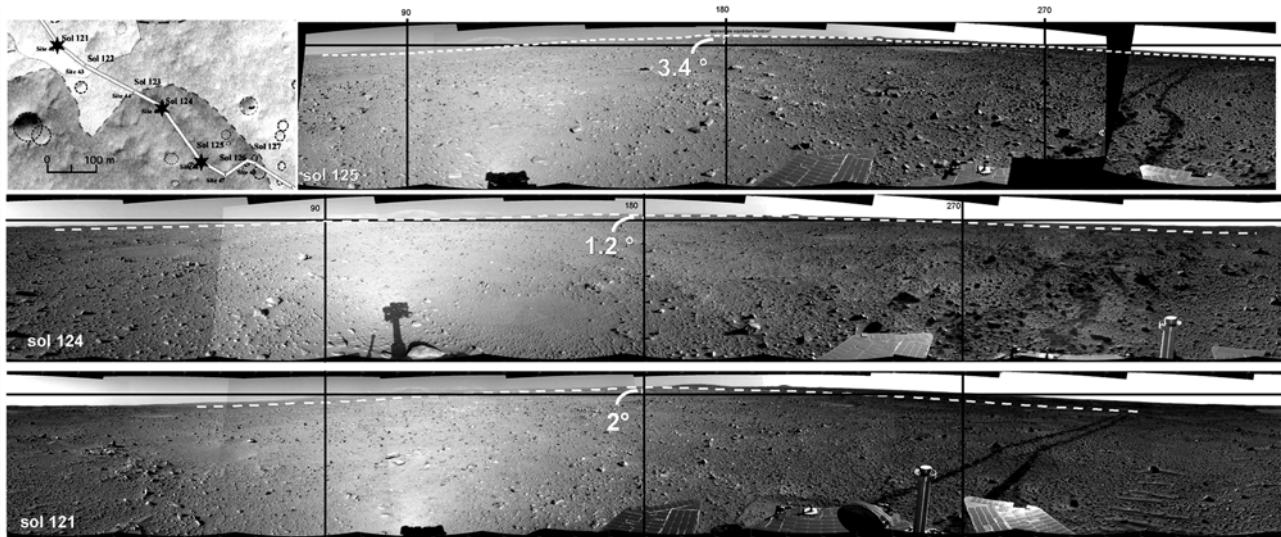
Figure 7. Navcam panoramas at sols 121, 124, and 125 and reference image showing traverse locations. The local horizon is closer, and the surface is elevated to the south relative to the north. These locations are near the northern edge of the tabled terrain. This suggests that the surface slopes from south to north and is relatively low relief. Navcam mosaics 2NN121EFF42CYL04P1827L000M1, 2NN124EFF45CYL00P1827L000M1, and 2NN125EFF46CYL00P1827L000M1.

morphologic map units. Where the traverse briefly crosses the tabled terrain between sols 123 to sol 127, the maximum relief is attained. Thereafter the traverse parallels the contact between the tabled terrain to the south and the transitional surface until sol 142 where the surface relief is minimal. After sol 142 the traverse crosses the whale-backed terrain where the surface descends to its lowest elevation before

reascending the blocky rise that marks another transitional zone, this one between the plains and the Columbia Hills.

2.5. Origin of Tabled Terrain

[21] The manner in which the relief varies and the distinctions in surface texture, which appear to correlate with the variations in relief, is comparable to many relief
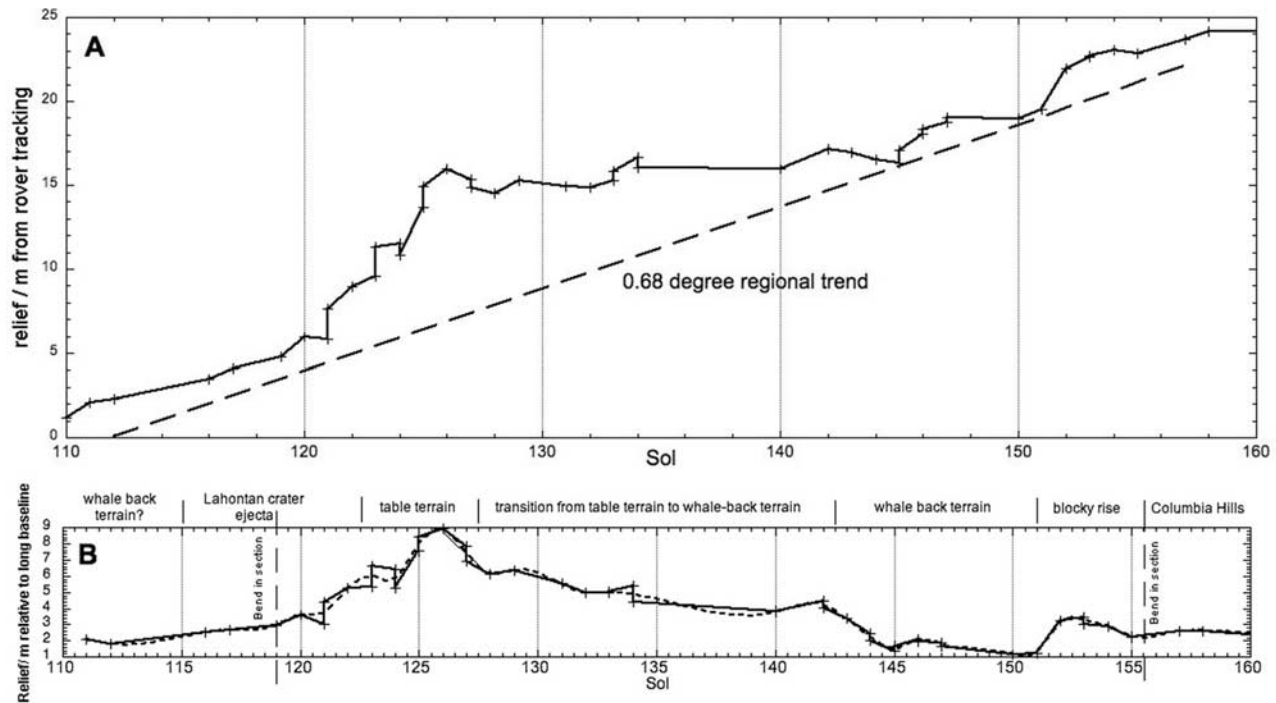
Figure 8. Relief measured from rover tracking from sol 110 to sol 160 [Li et al., 2006]. (a) The traverse ascended ~22 m over a regional gradient of about 0.68°. (b) Residual relief after removal of the regional trend. Prominent relief features correspond to morphologic terrains mapped from MOC image data.
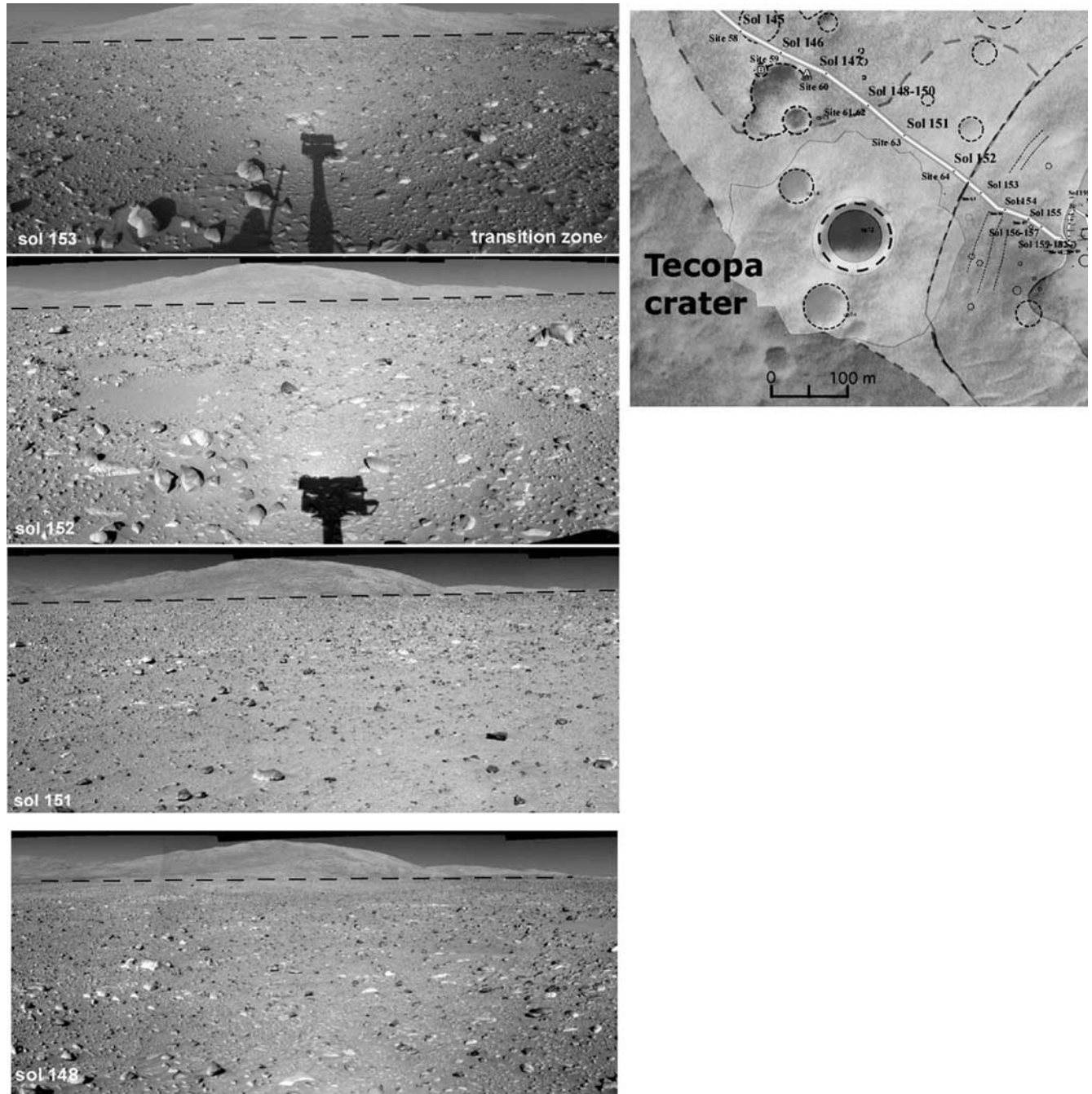
Figure 9. Successive Navcam images of the contact between the plains and the transition zone on sols 148, 151, 152, and 153 and reference image showing traverse locations. The dashed line indicates the slope from south to north across the ridge-like form of the transition zone. Navcam mosaics 2NN148EFF61CYL04P1826L000M1, 2NN151EFF63CYL00P1826L000M1, 2NN152EFF64CYL06P1826L000M1, and 2NN153EFF65CYP00P1826L000M1.

characteristics of terrestrial lava flows, including the superposition of local relief from multiple flow units onto a regional cross-flow gradient [*Zimbelman and Johnston*, 2001]. The tabled terrain is similar to the upper inflated surfaces of lava flows, where local relief may be complex and consist of generally planar elevated table-like surfaces defined by intervening collapse depressions. The latter point suggests that some fraction of the circular depressions may be primary lava flow relief features [*Greeley and Gault*,

1979] rather than degraded impact craters, a concept first considered for lunar maria during intial exploration of the Moon [*Kuiper*, 1966].

[22] Inflation plateaus occur when the internal pressure from the continued supply of lava to a flow front is insufficient to overcome the yield strength of flow margins and the surface of the flow is lifted (inflated) by continued influx of lava beneath a confining crust [*Walker*, 1991; *Hon et al.*, 1994]. Subsequent draining or differential deflation
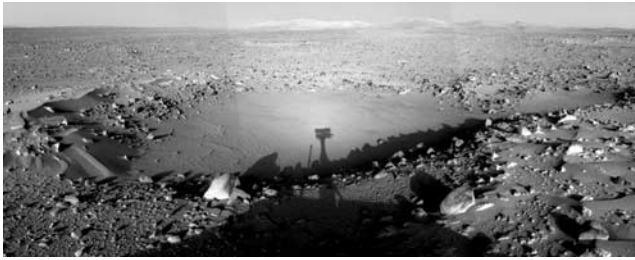
Figure 10. Navcam image of sediment-filled hollow and rocky rim, with shadow of the rover and imaging mast acquired at the end of the sol 111 traverse. The adjoining smaller hollow on the rim and single large block on the near rim are typical of many hollows. This hollow is also shown in Figure 11b. Note the rocky plain and Columbia Hills on the horizon. From image mosaic 2NN111EFF36CYL00P1818L000M1.

and cooling of the inflated surface results in complex collapse features often characterized by an accordance of elevation of intervening plateaus. The margins of the inflated area are controlled by the general margins of the flow such that the inflation occurs in the core region of a given flow unit. The resulting inflated region may have the appearance of a separate lava flow unit, including an undulating margin in map view and lobe-like offshoots. In addition to relief characteristics, the margins of inflation plateaus are often the site of small extrusions and breakouts from the inflated interior giving rise to small flow lobes and tongues of lava that can locally mimic pillow lavas [*Walker*, 1991; *Hon et al.*, 1994]. In this interpretation, the whale back terrain represents portions of the flow where less inflation and/or corresponding deflation has occurred.

[23] Inflated areas occur in lava flows frequently where the underlying surface gradient decreases relative to the upstream portions of the flow, such as when a flow encounters a barrier, temporarily ponds, and spreads laterally around the obstacle [*Walker*, 1991; *Hon et al.*, 1994]. An inflated area in the plains lavas west of the Columbia Hills might have arisen during emplacement if the basalts flowed from south-southwest, encountered the ridge line of the Columbia Hills, and locally ponded or inflated before flowing to the north and east around the north and south ends of the Hills.

2.6. Transition Zone

[24] A distinct "halo" terrain or transition zone occurs within the plains materials surrounding the Columbia Hills based on mapping from MOC image data. The transition zone (unit tz in Figure 5) is up to 200 m wide and consists of light and darker bands subparallel to the contact between the plains and the Columbia Hills. At the scale of the rover, the transition zone was characterized by a series of ridges and troughs that continued up to the contact with the hills. The ridge and trough character of the surface corresponds both with the transition zone as mapped in MOC image data and a slight topographic rise. The contact between the plains and the transition material that appeared sharp in maps prepared prior to the traverse was crossed on sol 152 to 153 without apparent differences in the clast characteristics, surface albedo, or larger-scale texture on either side of the

contact other than the transition to the ridges and troughs (Figure 9).

[25] Spirit traversed, but did not examine the ridge and trough terrain in detail. The characteristics of the clasts are insufficiently known to adequately assess hypotheses for the origin of this terrain. On the basis of broadly similar transition or boundary zones between the interiors of lava flow fields and adjacent preexisting countryside, one strong candidate for the ridges and troughs are pressure ridges and marginal fractures. In addition to potentially yielding an undulating surface once the ridges and cracks were sufficiently degraded over geologic time, marginal boundary zones on many flow fields may be elevated with respect to the flow interior due to dynamic inflation during flow emplacement.
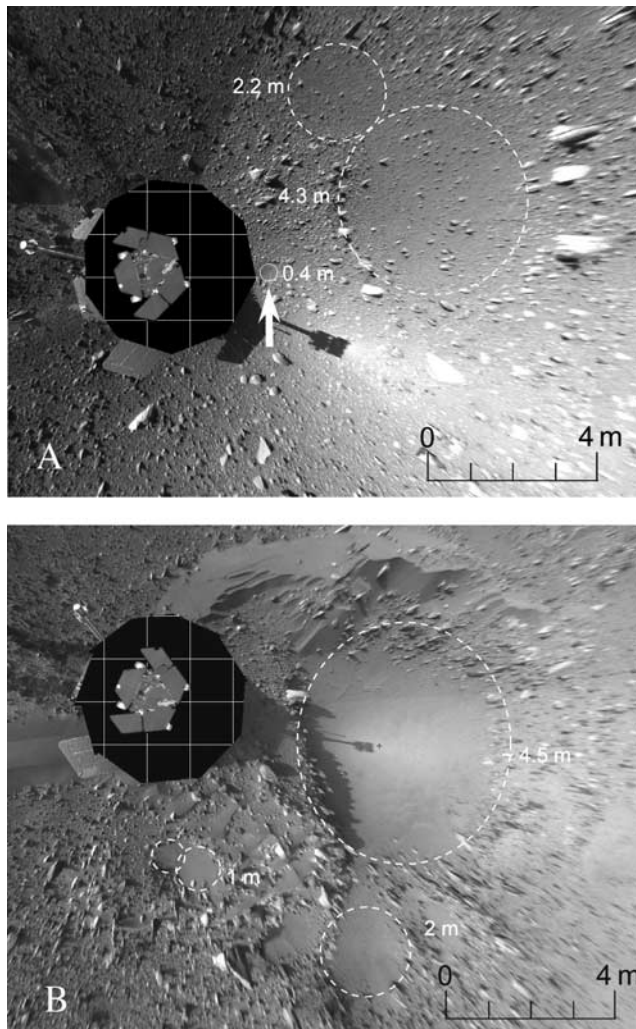
3. Hollows

3.1. Hollows From Rover Perspective

[26] "Hollows" are circular soil-filled depressions, typically with rocky rims that are ubiquitous on the plains surface. Hollows range in scale from tens of centimeters to tens of meters (approximately 50 m) in diameter, and consist of shallow depressions in which the abundance of small clasts and blocks is significantly less than the surrounding surface. The primary morphological criteria for their identification as small impact craters is their general circular plan and typically rocky rims (Figure 10). Raised rims and miniature patterns of ejecta that are more obviously expressed in larger ($\gg$50 m) craters are relatively uncommon and occur in only the larger and more youthful examples.

[27] From the rover perspective, hollows are characterized by two obvious forms: (1) generally circular patches of bright fines set in a field of rocky surroundings in which relief may or may not be perceptible as distance increases and (2) depressions with rocky rims and fines-covered floors; in some cases the relief and differences in texture between near and far rocky rims may be more apparent than the bright floor (Figure 11). Almost universally, when each hollow identified from rover perspective is located in MOC image data it appears darker in the MOC image than the surroundings (e.g., Figure 2).

[28] In the absence of obvious rims or depressions, many hollows are difficult to distinguish from the surrounding plains surface and are frequently defined as a circular region over which the rock size-frequency distribution is less than the surroundings. An example is the 4.3 meter hollow shown in Figures 10 and 11b from sol 111. In this case the rock abundance on the floor of the hollow is 3% by area compared with over 10% rock abundance outside the hollow (Figure 12). An increase in the rock abundance by a factor of three would be sufficient to completely obscure this hollow. Thus an age progression in hollows might follow from an initially deep depression with a rim of rocky debris to a slight depression largely filled with fines and ballistically emplaced rocks in which the size-frequency approaches the regional surface mean. Once the rock abundance on the floor attains regional values the hollow becomes essentially an undetectable extremely shallow depression in the surface that is indistinguishable from local relief variations. Relatively youthful examples are well

Figure 11. Hollows occurring as generally circular patches of fines in (a) shallow depressions to (b) deep depressions rimmed with rocky debris. These extremes of characteristics probably represent older infilled and late fresh hollows, respectively. All hollows have floors that are covered to variable extents by fine-grained material. Older hollows may be filled nearly to the rim with both fine material and later clasts of ejecta emplaced from subsequent impacts. Note that the large hollow in Figure 11b is the same hollow shown in Figure 10. The 40-cm-diameter circular depression (arrow) in Figure 11a is the smallest hollow detected over the course of the traverse. Image in Figure 11a is from sol 147, a part of Navcam mosaic 2NN147EFF60VRT02P1826L000M1; image in Figure 11b is from sol 111, a part of Navcam mosaic 2NN111EFF36VRT00P1818L000M1.

illustrated by several larger hollows encountered along the plains traverse between sols 110 and 112 (Figure 13).

[29] Complex hollows (Figure 14) are common and are typified by clusters of small depressions, frequently overlapping and in general confusing the circularity of the largest hollow within the cluster. Two scenes are shown from a position north and north east of the hollow complex with respective features (D, F, and G) identified from the two perspectives. Note also that the Navcam sol 147 scene

shown in Figure 11a is from the position located on the northeast and within 2 hollow radii of the larger hollow. The rock abundance in this location is 10% and thus the ejecta from the larger hollow is not readily distinguishable from the background plains rock abundance even at this close proximity to a relatively larger hollow.

3.2. Hollows and Crater Abundance in Plains

[30] The crater size-frequency distribution for the plains surface was determined from measurements in MOC images for craters in the size range 10 m to 600 m in 31 km^2 area located around the landing site and containing the area traversed (Figures 15 and 2). Measurements of hollows along the traverse enabled the first crater counts determined from a ground survey on Mars and include impact craters down to a scale of tens of centimeters. This provides an extension of size-frequency measurements based on orbital image data to diameters well below that previously possible.

[31] The diameters and locations of hollows along the traverse during the first 90 sols were measured from perspective views and in vertically projected (i.e., map projected) Navcam panoramic mosaics (e.g., Figure 11). Perspective measurements made use of the visualization and measurement tools available in the Mars Exploration Rover (MER) Project Science Activity Planner (SAP) [*Norris et al.*, 2005] and enabled stereoscopic viewing and ranging measurements. The range and azimuth to the apparent center of candidate hollows and the horizontal distances to the left and right points of the rim were measured using SAP, and a representative circle was mapped in site frame on an overhead view map. Once all of the apparent hollows at a given site were measured and mapped, they were
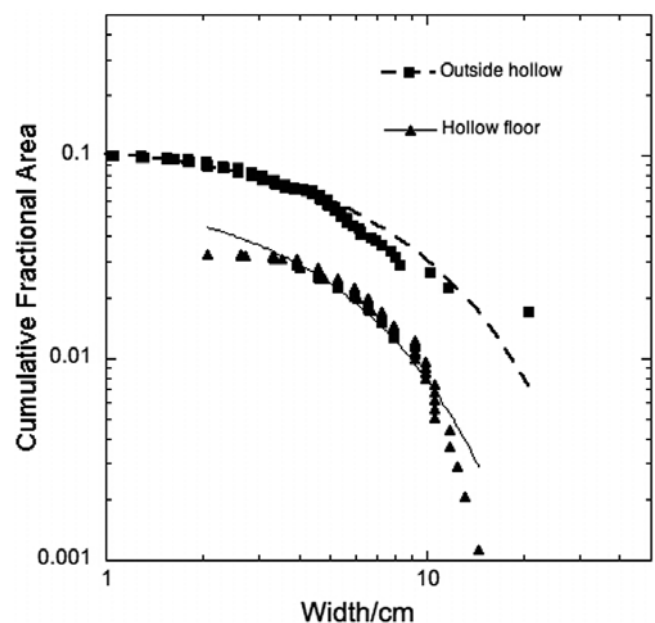
Figure 12. Rock size-frequency distribution on the floor and outside the 4.3 m hollow illustrated in Figures 10 and 11b. The interior rock abundance is about 3% (cumulative area covered by rocks), whereas the surrounding rock abundance is 10%. An additional 6–7% of rocks contributed by ejecta from a local impact would make this hollow practically undetectable.
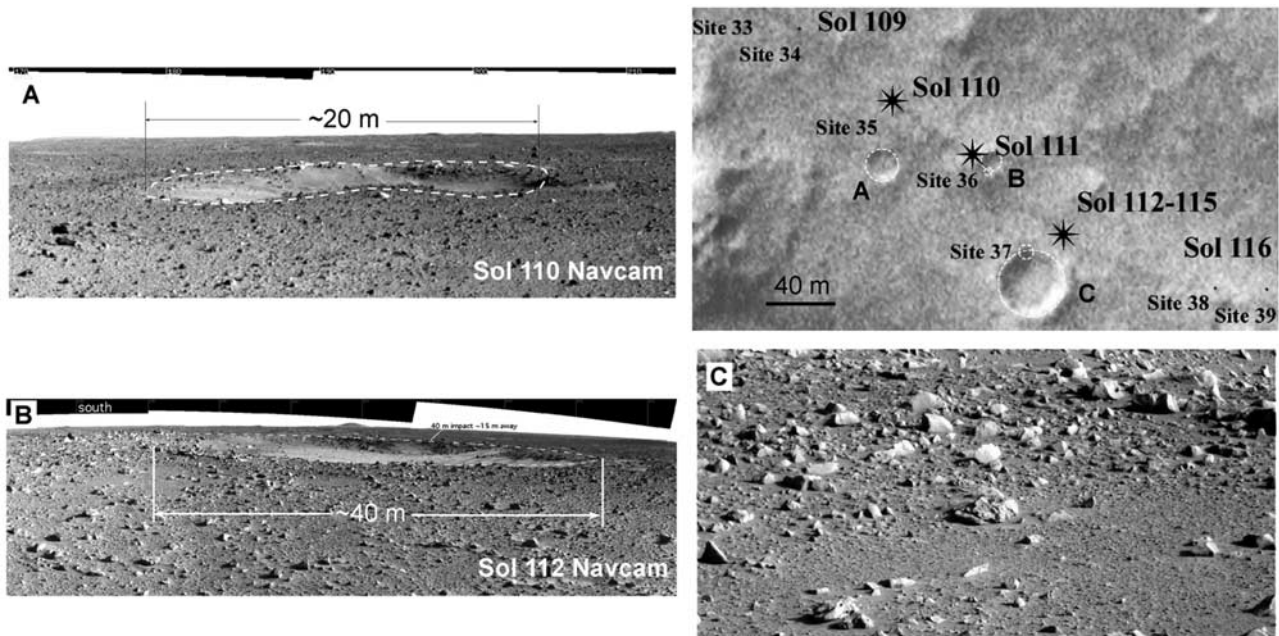
Figure 13. Representative hollows as imaged from the ground and encountered between sols 110 and 112. Image map of traverse location on right is from MGS MOC release number MOC2-960. (a) A 20 m hollow located approximately 40 m south of the sol 110 position. The undulating profile of the rim probably reflects local variations in relief that predate the hollow, which is of the same order as relief associated with the actual rim. Navcam image mosaic 2NN110EFF35CYL00P1818L000M1. (b) Forty meter hollow south of the sol 112 position. In this case the rim ejecta on the east rim is significantly greater, implying a slight asymmetry in the formation. Note that as in Figure 13a, a single small hollow of similar degradational state occurs on the northwest rim. From image mosaic 2NN 112EFF37CYL00P1818L000M1. (c) Pancam subframe (2P136498000ESF37CAP2562L7M1) of the east (left rim) proximal ejecta of hollow shown in Figure 13b.

compared with the corresponding vertically projected Navcam mosaic.

[32] In practice, two types of disparity were common: (1) hollows measured and positioned from SAP often disagreed in diameter and position with measurements as determined in vertically projected Navcam mosaics and (2) some hollows that were readily apparent in Navcam vertically projected mosaics were not identified in perspective views. The first type of disagreement could be a result of the inability to correctly identify the vertically projected center
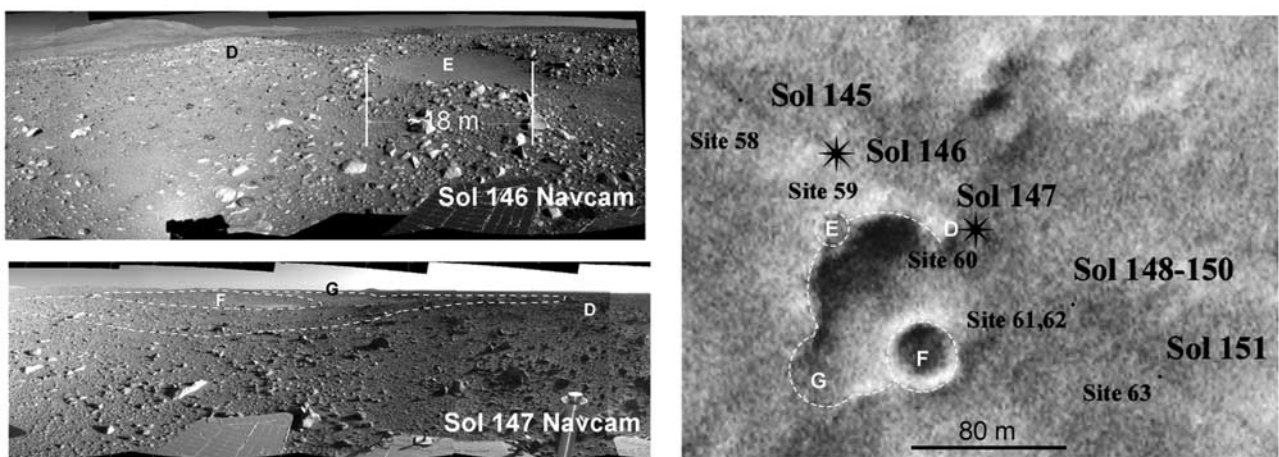
Figure 14. Complex hollow as imaged from the ground and encountered between sols 146 and 147 and traverse locations in MOC image. Letters correspond to individual hollows shown in background MOC image (R15-02643 and R20-01024.50a) to the right. Panoramic mosaics are from 2NN146EFF59CYL06P1826L000M1 and 2NN147EFF60CYL02P1826L000M1. Image of the surface surrounding the rover at the sol 147 position (site 60) is shown in Figure 10.
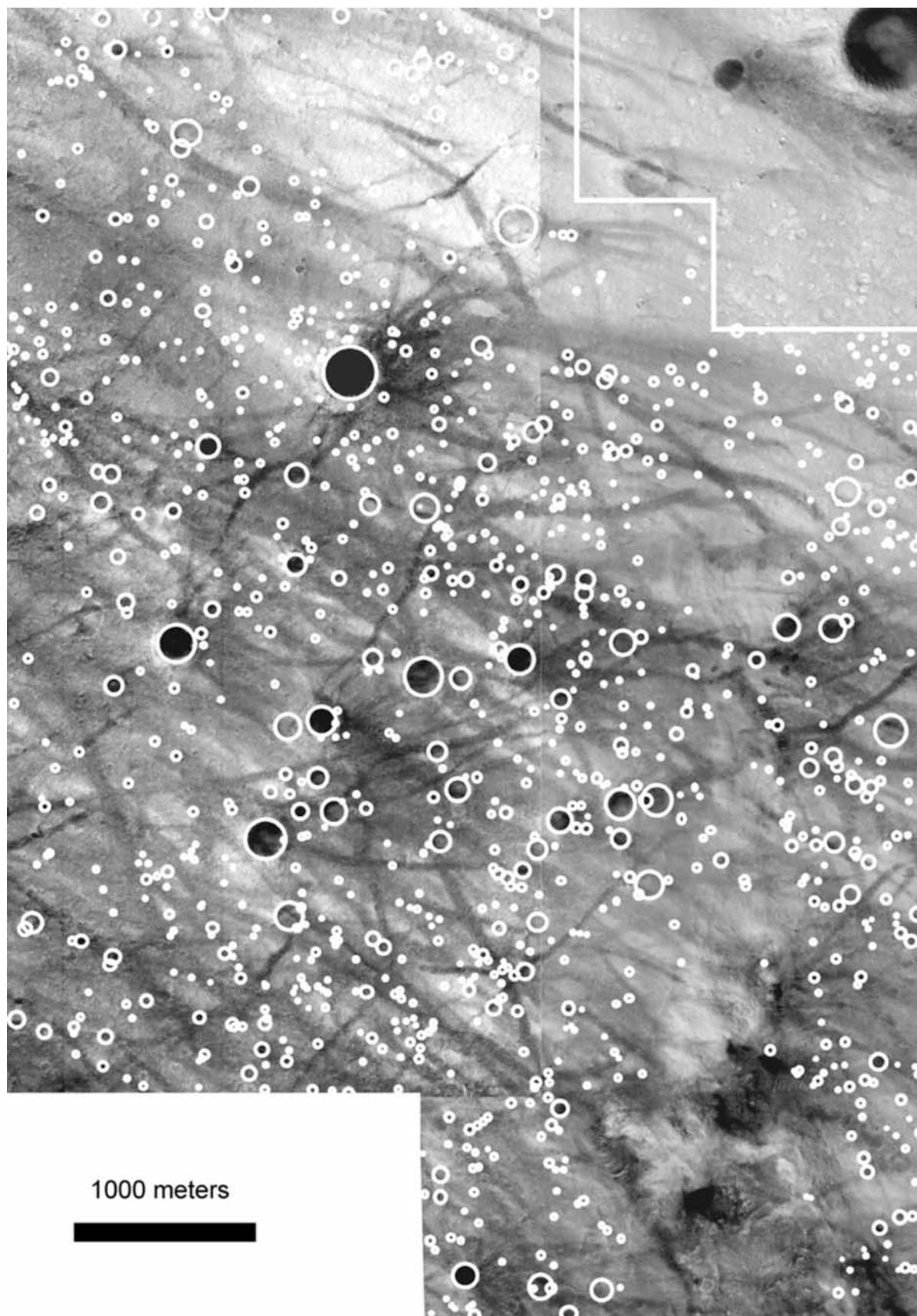
Figure 15. Regional image of all identifiable small impact craters (between 10 and 600 m in diameter) in the vicinity of the Spirit landing site. Image without the craters circled is Figure 2. MOC images R07-01606 and R13-01467; north is up.
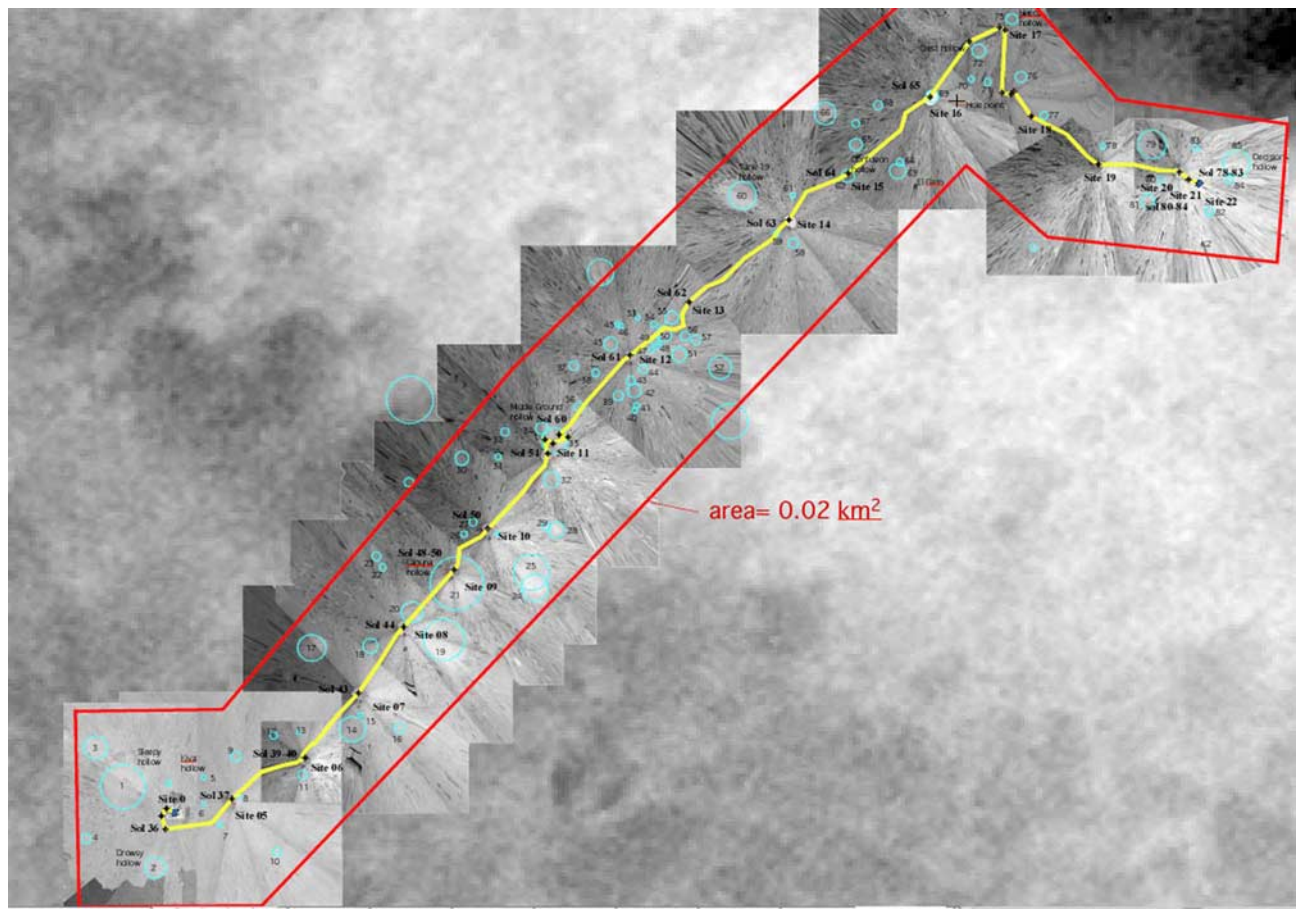
Figure 16. Map of all hollows identified from the ground between the lander and the position at sol 90. The map width is defined as the width of standard Navcam vertical mosaics centered on the rover position (40 m). Background image is a composite of MOC images R13-03051 and R13-01467.

of each hollow from the oblique perspective, thus leading to incorrect ranging of the center of the hollow. Similarly, linear measurements perpendicular to the line of sight typically suffered when the selected points were in reality too far or too near with respect to the actual rim of each hollow.

[33] The second type of disagreement between perspective and vertical views arises from the fact that many hollows are only detectable as circular patches of fines in perspective views, such as where the near rims obscure the floors. In addition, hollow detection was easier from the vertical projection because it enabled better discrimination of the generally circular patterns of sediment fill and clast abundance, in particular the aggregation of larger rim clasts and blocks.

[34] The ranging estimates provided by perspective views should in theory be more accurate at defining dimensions and locations of hollows than vertically projected mosaics, as the mosaic algorithm used for vertical projections assumed for simplicity a planar surface and does not account for variations in relief along the line of sight. Despite this, the final hollow distribution map was done with vertically projected mosaics, given that identifying hollows was more consistent and the corresponding diameters better constrained. Perspective-based information was used to validate the identification.

[35] The area over which actual measurements were made was determined by the limit of accurate Navcam ranging

(20 m from the rover), but largely defined by the standard dimension of the Navcam vertical mosaic products (40 m by 40 m). During the first 90 sols the map projected Navcam mosaics overlap such that a "mapping corridor" 40 m wide, centered along the rover traverse can be defined. The area of this corridor from the lander to the position at sol 90 (0.018 km^2) is defined as the area counted (Figure 16).

[36] SAP ranging methods (subject to all the uncertainties just described) were used in determining the depths of hollows over the same traverse interval. Hollow depths relative to diameters vary over an order of magnitude between 0.2 and 0.02 times hollow diameter (Figure 17). Apparent rim heights likewise vary over an order of magnitude from 0.5 to 0.05 hollow diameters. These variations are consistent with the range of apparent degradation states and with possible differences in impact energy during formation.

[37] The cumulative number per km^2 versus diameter plot of the hollow data from the rover and the crater data from orbit display power law distributions generally similar to those measured for impact craters from orbit (Figure 18). The power law slope for the craters is −2, which matches the usual −2 power law expected for larger craters from orbit [*Tanaka*, 1986]. The power law slope for hollows is slightly lower at −1.5, but both distributions appear continuous with the largest hollow (∼10 m diameter) falling near the smallest crater at ∼100/km^2. The relatively low slope of the hollow distribution is consistent with the
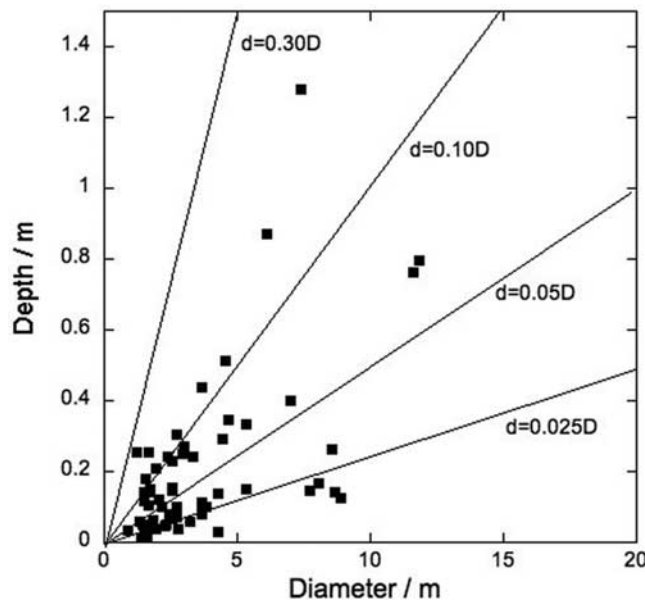
Figure 17. Hollow depth-diameter measurements from the Science Activity Planner (SAP) in Navcam stereo images. Lines show different depth/diameter (d/D) relationships. Only 4 of the 58 hollows are substantially deeper than 0.1D, suggesting original shallow depths.

preferential loss of smaller hollows due to resurfacing (section 3.1). Nevertheless, the cumulative number of craters at N(1 km) is slightly larger than typical of Hesperian surfaces [e.g., *Hartmann and Neukum*, 2001]. These slightly higher crater abundances at small size relative to those expected from counts of larger craters over larger areas [e.g., *Kuzmin et al.*, 2000] may be an indication that many hollows and small craters are in fact secondaries (see discussion in section 4.2). Alternatively, as discussed in section 2, some of the craters included in the areal survey may be volcanic collapse features, thus contributing an additional unknown number of counts to the population of actual impact craters. Collapse depressions are common on many basalt flows on Earth and have size-frequency distributions similar to impact craters for diameters above 10 cm [*Greeley and Gault*, 1979]. The lower slope for hollows may be either a production characteristic or could reflect progressive loss of smaller hollows from the surface record by infilling and destruction from adjacent hollows. Regardless of the mechanism that is producing the slightly lower slope for hollows, the power law distribution and general similarity and continuity to distributions of impact craters measured from orbit strongly argues (along with their morphology) that hollows are modified impact craters and thus represent the first statistical sample of impact craters on Mars at meter scale.
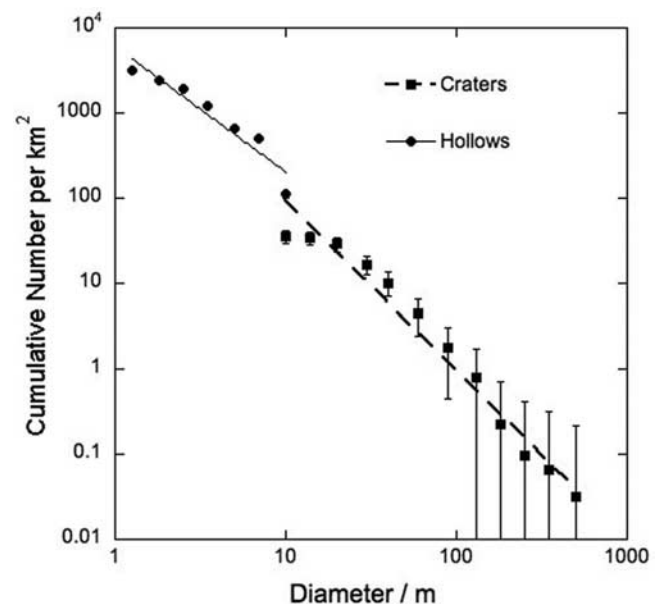
4. Craters

4.1. Large Craters

[38] Craters dominate relief on the Gusev plains, range in size from less than a meter to over 200 meters in diameter, and when fresh are simple bowl-shaped structures. Larger craters typically possess meters of relief and are surrounded by readily mapped ejecta deposits. Four craters ~100

meters in diameter were investigated during the Sprit rover traverse (Figure 5) and include Bonneville (210 m diameter), Missoula (163 m diameter), Lahontan (90 m diameter), and Searles crater located west of Lahontan (~100 m diameter). Tecopa crater, near the Columbia Hills, is ~100 m diameter and was not closely approached and only the ejecta was assessed.

[39] The 210 m diameter Bonneville crater has a raised rim reaching 4.1 to 6.4 m above the surrounding plain, but lacks pronounced relief along its perimeter. The crater averages 10 m deep with a maximum floor-to-rim-crest relief of 14 m (Figure 19a). Interior walls are generally smooth at the 5–10 m scale, slope an average of 11°, are usually concave upward, and are not bounded by extensive talus (Figure 19b). Eolian drift mantling the floor of Bonneville is likely only a few meters thick, as rocks protrude in many locations. Bonneville's ejecta deposit displays an abrupt and easily mapped distal margin, an exponential increase in number of rocks with decreasing size, and the maximum size of constituent rocks increases fivefold up to the rim crest from 0.5 m to 2.5 m in diameter [*Grant et al.*, 2004; *Crumpler et al.*, 2005]. These characteristics indicate Bonneville is the freshest large crater visited by Spirit.

[40] Missoula crater is 163 m in diameter, only 3–4 m deep, and retains a ~3-m-high raised rim. Walls slope approximately 6° and appear smooth and devoid of talus or debris chutes. Missoula is more filled than Bonneville by eolian deposits, ejecta from a large hollow on the northeast rim, and some rocks that may be ejecta from Bonneville. The size frequency distribution of the near-rim ejecta frag-

Figure 18. Size-frequency distribution of 58 hollows between 0.9 m and 12 m over the 0.018 km² area characterized by the surface transect and all impact craters (total number 1098) between 10 m and 600 m in a 31 km² plains region in MOC images that includes the plains traverse (Figure 15). Power law fit to hollow data yields diameter exponent of −1.47 (R = 0.96); power law fit to crater data yields diameter exponent of −1.98 (R = 0.87). Error bar is standard square root of the average bin diameter.
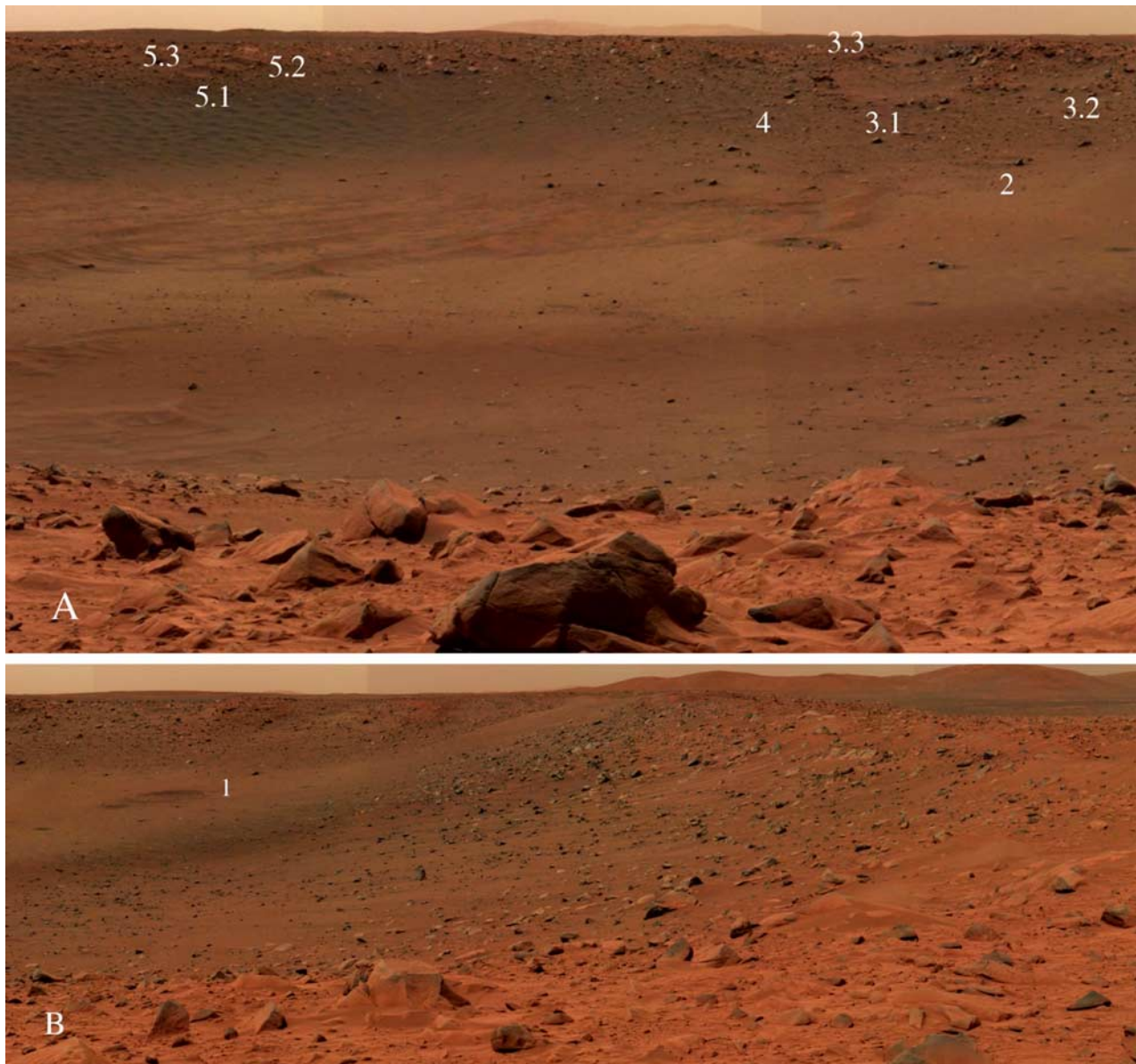
Figure 19. Pancam mosaic of portion of Bonneville crater. (a) Central portion of crater (40°–70°) shows sediment and drifts on floor and far wall as well as rocky rim impacted by small crater triplets. Sediment on floor is limited in thickness by partially buried rocks. Small numbered craters have morphometric data in Table 1. (b) Eastern part of Bonneville crater (70°–120°) shows blocky and dusty rim and shallow sloping wall composed of jumbled rocks and no outcrop. The exposed walls show no obvious signs of mass wasting, suggesting that the exposed crater form is relatively pristine and that the shallow walls and depth resulted from impact into a cohesionless regolith of ejected rubble. Note small crater 1 on the floor and Columbia Hills on the horizon.

ments at Missoula is similar to the distribution observed at Bonneville, but largest fragments are just over 1.5 m in diameter.

[41] Lahontan crater is 90 m in diameter, has a rim height of ~2–3 m, walls sloping at an average of 6°–7°, a depth of up to 4.5 m (Figure 20), and appears less filled than Missoula. Searles crater west of Lahontan is ~100 m in diameter, possesses only 1–2 m of relief, and is mainly filled by deposits similar in appearance to those in Missoula and may be a mix of eolian sediments and ejecta blocks. Rim outlines of all these craters are uniform (though poorly circular from orbit (Figure 2)), walls are smooth and low sloping, and ejecta rock size distributions are similar to Bonneville and Missoula to first order.

[42] Development of the gradation history of the cratered plains surface in Gusev [Grant et al., 2004] and comparisons to the modification of terrestrial impact craters argues that crater formation into basaltic rubble creates a landform comprising variably sized rock fragments whose rim and ejecta surfaces are in disequilibrium with the long-term gradational setting [Grant et al., 2006]. Initially, a geologically brief period of eolian activity modifies crater surfaces,

Figure 20. Navcam image of shallow, sediment-filled Lahontan crater. Lahontan is 90 m in diameter, has a rim height of $\sim$2–3 m, shallow walls sloping at an average of $6°$–$7°$, and depth of up to 4 m. Note large, bright (dusty) drift and rocky surface. Navcam image 2N137028119FFL100P1827L taken on sol 120.

causing deflation of up to tens of centimeters of fines and formation of lag deposits that slows additional erosion. Some of the transported fines are trapped and deposited within the craters and account for infilling and the creation of hollows. Initial postimpact eolian activity is likely accompanied by some mass wasting as rubble-mantled crater walls stabilize, but an absence of gradation signatures associated with significant mass wasting (e.g., debris chutes and talus) indicates the process is short lived and not responsible for appreciable changes in form. Long-term gradation is slowed by the limited supply of sediments suitable for eolian transport made available by slow weathering of basaltic clasts and disruption of armored surfaces during subsequent impacts. Although water related weathering may contribute some fines for eolian transport and some limited colluvial activity, it has not induced runoff and plays a minimal role in crater gradation in Gusev. Overall, the relatively pristine nature of many of the larger craters coupled with low depth-to-diameter ratios of <0.1 imply the craters are relatively pristine secondaries formed into a disrupted basaltic lava plain [*Grant et al.*, 2004, 2006] (see next section).

[43] The MOC orbital view of the Gusev plains craters $\sim$100 m in diameter and larger contrasts somewhat with the view from the surface. MOC reveals (Figure 2) shallow, subdued craters, with poorly circular planforms, lacking obvious, blocky ejecta deposits that typically appear relatively degraded [*McEwen et al.*, 2005]. Moreover, orbital image resolution is insufficient to completely resolve small craters in the southeast wall of Bonneville and suggests the presence of crenulations or spurs that might lead to erroneous interpretation that mass wasting is important in modification of the craters. As discussed in the next section, these characteristics are resolvable if the craters are relatively fresh secondaries that have undergone much less modification, other than filling in by sediment and deflation of ejecta.

4.2. Crater and Hollow Morphometry: Secondaries

[44] The poorly circular planforms, low depth-to-diameter ratios, and shallow wall gradients for the Gusev craters are most consistent with fairly pristine secondary craters formed

into unconsolidated rubble. The expected depth-to-diameter ratio (d/D) of fresh primary craters on the Moon and Mars is about 0.2 and the rim height/diameter ratio is 0.04 [*Pike*, 1977]. A summary of crater geometries from MOLA data [*Garvin et al.*, 2003] reports an average $d = 0.21D^{0.81}$ for simple craters with variations ascribed to different target terrains, which predicts d/D of 0.3 for 100 m diameter primary craters. However, these estimates are extrapolations from measurements of larger craters and smaller lunar primary craters have d/D ratios of 0.2 [*Wood and Andersson*, 1978], so that 0.2 d/D is the best estimate for small primary craters on Mars. *Pike and Wilhelms* [1978] carefully measured the shapes of 150 craters on the Moon that could confidently be identified as secondaries (from spatial distribution, clustering, and identification of the primary crater) with diameters of 43–200 m. They found the secondaries to be markedly less circular and to have shallower depth/diameter ratios ($\sim$0.1) and lower rim height versus diameter ratios (0.02), all of which are consistent with the expected lower-impact velocities, lower-impact energies, oblique impact angles and clustered impacts.

[45] Prior to landing, high-resolution digital topographic maps [*Kirk et al.*, 2003] of MOC images of craters on the Gusev plains showed that they had morphometric characteristics consistent with those expected for secondary craters [*Hurst et al.*, 2004], most of which could be distant and difficult or impossible to trace to a particular primary crater [*McEwen et al.*, 2005]. Depth/diameter ratios of over 500 craters with diameters from 10 m to 500 m measured in the highest-resolution digital elevation models ($\sim$3 m) of the Gusev plains had average d/D of 0.03 to 0.1, but the freshest craters had d/D of 0.1. In addition, the average rim height versus diameter ratio for the freshest craters is intermediate (0.033) between that measured for secondaries and primaries. With the perspective gained from Spirit's traverse, the freshest crater on the ground, Bonneville has a d/D (0.07) that is similar to the freshest craters from orbit ($\sim$0.1) and the lower d/D craters have been filled in by eolian material. Bonneville would require only a few meters of fill to account for the observed d/D ratio from an initial 0.1 d/D. Similarly, Lahontan (d/D = 0.05) may be filled by as little as 3–4 m of sediment, consistent with the numerous rocks still visible on the crater floor. At the more degraded Missoula, $\sim$10 m of fill could account for the current d/D ratio of only 0.03 if the crater is a secondary [*Grant et al.*, 2006]. The observed average rim height versus diameter ratio of Bonneville, Lahontan, and Missoula (0.035) is also similar to that observed in the freshest small Gusev craters from orbit (0.033). Although intermediate between primary and secondary lunar craters, it is possible that rim heights are influenced by properties of the target materials and so the observed heights could be consistent with secondary impacts into blocky regolith. In any case, the observation that large craters observed by MER have values of d/D that match secondaries on the Moon for a similar range of diameters argues that the Gusev craters are also secondaries.

[46] Spirit's observations of hollows are also consistent with their being mostly secondaries. Many hollows form in clusters (section 3.1, Figure 14) with overlapping, poorly round planforms and irregular rims, all common characteristics of secondaries [e.g., *McEwen et al.*, 2005]. The measured d/D of hollows (Figure 17) shows most hollows

Table 1. Morphometry of Small Craters Superposed on Bonneville[a]

Crater	Diameter (D), m	Depth (d), m	d/D	Rim Height (R$_h$), m	R$_h$/D
1	10	0.5	0.05	0.5	0.05
2	7	0.5	0.07	0.25	0.04
3.1	13	0.4	0.03		
3.2	12	1.1	0.09		
3.3	12	0.6	0.05		
4	5	0.4	0.08	0.2	0.04
5.1	10	0.5	0.05	0.3	0.03
5.2	15	0.5	0.03	0.2	0.01
5.3	15	0.5	0.03	0.3	0.02

[a]Location of craters identified in Figure 19.

with diameters from 1 m to 12 m have d/D that are less than 0.1. Only 4 of 58 hollows measured are appreciably deeper than the d/D = 0.1 line, suggesting most hollows formed as shallow craters and then become shallower by being filled in by sediment. The shallow d/D of the deepest hollows suggests that like the larger craters observed by Spirit, the smaller ones are also secondaries.

[47] The morphometry and form of the freshest small craters observed by Spirit also argues that they are secondaries. There are about 12 small craters between 5 and 20 m diameter that have impacted into the rim and floor of Bonneville (Figure 19), which is the freshest large crater. Nine of these form triplets of 3 overlapping crater clusters that resemble what might be expected for coeval secondaries. Others form on the aeolian fill in the bottom. All have a fresh, unmodified appearance and those on the floor have sharp rims. The craters in the clusters have distinctly noncircular planforms. Although the craters are far enough away to be near the limit of reliable stereo measurements, a handful of careful measurements of crater diameter, depth and rim height were made for each [*Li et al.*, 2006] with results presented in Table 1. All craters are extremely shallow with d/D ratios of less than 0.1 with an average of 0.05. Rim height/depth ratios are more variable, but average 0.03, which is consistent with the larger craters observed from the ground and from orbit. Depth/diameter ratios <0.1 are much more consistent with secondary craters [*Pike and Wilhelms*, 1978; *Hurst et al.*, 2004; *McEwen et al.*, 2005] than primaries and the noncircular planforms and clusters similarly argue that the freshest craters observed at Gusev are secondary craters. Because the cratered plains of Gusev can be considered as a representative sample of Hesperian cratered terrain (similar morphometric results are reported for small craters in similar aged terrain in Isidis Planitia [*Hurst et al.*, 2004; *McEwen et al.*, 2005]) and if most of the small craters on Hesperian plains are secondaries like those observed by Spirit, then it raises important questions concerning the use of small craters for dating surfaces and for estimating regolith production and quantifying erosion (see discussion of *McEwen et al.* [2005]).

5. Rocks

5.1. Introduction

[48] Most rocks appear dark, fine-grained, pitted, angular to subangular and almost none display obvious rounding. Most appear coated with dust and some lighter toned rocks have thin weathering rinds whose formation may have involved small amounts of water [*McSween et al.*, 2004]. Rocks that are sitting or "perched" on the surface and are largely exposed are 2–10 times more numerous around the margins of hollows than elsewhere and are accompanied by anomalously high concentrations of rocks that appear fractured or split into multiple fragments [*Grant et al.*, 2004]. Occasionally, the perched and fractured or split rocks contribute to block concentrations that are crudely radial to the hollows. By contrast, the lower interior of the hollows and local drift deposits are noticeably devoid of rocks larger than ~15 cm in diameter and faceted rocks, some of which may be ventifacts, are 5–8 times more abundant away from hollows. Lighter toned (redder) rocks are often concentrated around local eolian drift accumulations and may reflect exhumation from beneath these deposits. These observations support the deflation of sediment around craters and the filling in of the craters to form hollows.

5.2. Methods

[49] There have been 3 different counts of rocks along the Sprit traverse that focus on different aspects of the rock population. Two focus on systematic measurements along the route using Pancam and Navcam images of small areas [*Crumpler et al.*, 2005; *Ward et al.*, 2005] and one focuses on much larger areas in portions of complete panoramas that capture the largest rocks [*Golombek et al.*, 2005a]. Rock counts were made by *Golombek et al.* [2005a] at three roughly 70° sectors of complete panoramas within 10 m of the rover at Mission Success (CMS) (8447 rocks in 56.9 m^2 area from 0° to 76°), Legacy (426 rocks in 58 m^2 area from 318° to 28°) and Bonneville (689 rocks in 84.1 m^2 area from 255° to 353°). Rocks in the panoramas were manually identified using an interactive Graphic User Interface of RockIT, a component of the OASIS software (Onboard Autonomous Science Investigation System) [*Castaño et al.*, 2004]. Range data was then used to calculate apparent width (1.33 times the diameter) and height [*Golombek and Rapp*, 1997; *Golombek et al.*, 2003b]. Because these counts were over much larger areas, they focus on larger rocks between 0.05 and 2 m in diameter at the Legacy and Bonneville sites and between ~0.01 and 2 m diameter at CMS.

[50] The *Crumpler et al.* [2005] counts were made in end-of-drive Navcam panoramas within a standard 2 m^2 subarea centered 1.5 m from the front of the camera mast. Single axis measurements of all clasts greater than ~2 cm were made in 36 images from Sol 12 to Sol 154, which resulted in typically 100–200 rocks per count. Because these counts used lower-resolution Navcam images over larger area, they focused on pebble to cobble size clasts (2–50 cm). Clast width was measured horizontally across each image perpendicular to the Navcam mast, producing a random sample of the diameter of the clast (assuming no preferred orientation). Results showed a relationship of rock abundance with distance from the Bonneville crater rim, lower rock abundances in intercrater plains [*Crumpler et al.*, 2005], and a positive relationship between rock abundance and thermal inertia [*Moersch et al.*, 2005].

[51] The *Ward et al.* [2005] counts were made in 14 systematic "clast survey" Pancam images along the traverse from Sol 13 near the lander to the edge of the Columbia
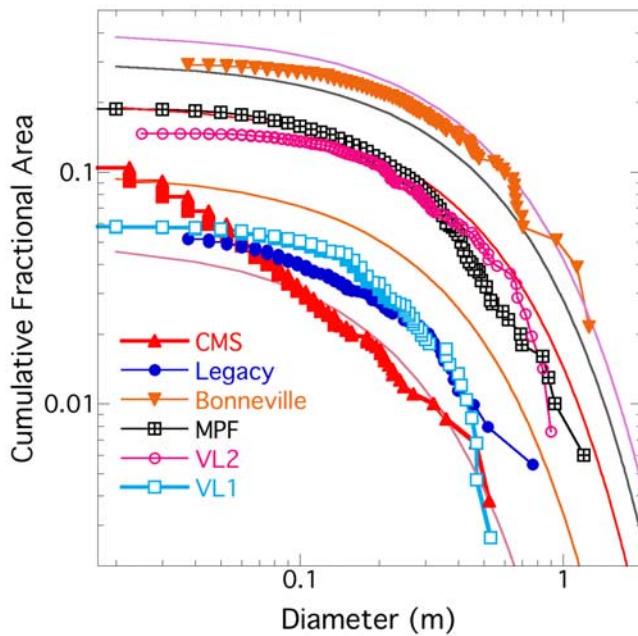
Figure 21. Cumulative fractional area versus diameter plots of rocks counted in portions of the Mission Success (CMS), Legacy, and Bonneville panoramas; Viking Lander (VL) and Mars Pathfinder (MPF) landing sites and model distributions are based on VL sites, and a rocky location on Earth [*Golombek and Rapp*, 1997] is shown for reference. Model distributions are for 5%, 10%, 20%, 30%, and 40% total rock abundance and can be distinguished based on where the curves intersect the ordinate, which is the cumulative fractional area covered by all rocks. See text for further discussion.

Hills on Sol 154. The long and short axes of all clasts greater than 1 mm were measured in small areas of average 0.2 m^2 (0.03–0.39 m^2), which produced an average of 314 rocks per area (106–725). Because of the use of high-resolution Pancam data over small areas, these counts focused on the size-frequency distribution of granule to pebble size clasts. The length and width of each clast were averaged to yield the diameter. Clasts on the intercrater plains are smaller, better sorted and more evenly spaced than those near crater rims [*Ward et al.*, 2005].

5.3. Results

5.3.1. Size-Frequency Distribution

[52] Results of the *Golombek et al.* [2005a] rock counts show 7%, 5% and 29% of the surface is covered by rocks greater than ~0.04 m diameter at the CMS, Legacy and Bonneville sites, respectively (Figure 21). The cumulative fractional area versus diameter plot shows the characteristic exponential decrease in fractional area covered by larger rocks observed at the Viking Lander (VL) and Pathfinder (MPF) landing sites [*Golombek and Rapp*, 1997]. The shape of these curves is similar to those found at the other landing sites on Mars as well as rocky sites on Earth [*Golombek and Rapp*, 1997] and has been ascribed to fracture and fragmentation theory [e.g., *Rosin and Rammler*, 1933; *Gilvarry*, 1961; *Gilvarry and Bergstrom*, 1961], which predicts that ubiquitous flaws or joints will lead to exponentially fewer

blocks with increasing size during ejection and transport [e.g., *Wohletz et al.*, 1989; *Brown and Wohletz*, 1995] (see *Golombek and Rapp* [1997] for further discussion). Equations of the form $F_k(D) = k \exp[-q(k) D]$ were derived from the VL1 and VL2 sites, that also accurately predicted the Pathfinder rock distribution [*Golombek et al.*, 2003b], where $F_k(D)$ is the cumulative fractional area covered by rocks of diameter D or larger, k is the total area covered by all rocks, and q(k), is the exponential that governs how abruptly the area covered by rocks decreases with increasing diameter [*Golombek and Rapp*, 1997].

[53] The size-frequency distribution of larger rocks (>0.1 m diameter) generally follows the exponential model distribution for total rock abundances of 5%, 7% and 35% at the three respective sites, although there are far more pebbles at the CMS (consistent with less bright dust and drift material at this site) than at other locations. The cumulative fractional area plot at CMS displays power law behavior from 0.1 to 0.03 m diameter, but flattens out at smaller diameters so that a total of about 11% of the surface is covered by rocks at this site, with about half of that covered by pebbles. The largest rock size in the counts increases as the rock abundance increases from 0.5 m to 0.8 m to 1.3 m diameter toward the rim of Bonneville crater. Average THEMIS thermal inertia (Figure 3) varies from 285 at the landing site, to 290 partway up the Bonneville ejecta, to 330 around Bonneville and show systematic variations that can be related to observed variations in rock abundance and material properties [*Christensen et al.*, 2004a; *Golombek et al.*, 2005a; *Fergason et al.*, 2006; *Moersch et al.*, 2005]. Adjusting the intermediate rock count upward [*Golombek et al.*, 2003b] to account for the difference in THEMIS bulk thermal inertia for the Legacy location (290) versus the average (306) (assuming that the difference is due to more rocks [*Moersch et al.*, 2005]), about 7% of the surface would be covered by rocks >0.1 m in diameter, which compares favorably with the orbital rock abundance estimate of 8% [*Christensen*, 1986]. For effective thermal inertias of rock populations [*Golombek et al.*, 2003b], the increase in bulk inertia on the Bonneville ejecta blanket is more than explained by the increase in rock abundance, and suggests a corresponding decrease in fine component inertia, which appears consistent with observations of more dust closer to the rim [*Golombek et al.*, 2005a].

[54] The observed decrease in rock abundance away from Bonneville is also consistent with expectations based on detailed block counts around small (<1 km) fresh lunar craters. The largest block expected at the rim of Bonneville (~2.5 m) is close to that expected based on the relationship between crater diameter and maximum ejecta size and the decrease in block size with distance is also consistent with that expected for a fresh crater [*Grant et al.*, 2004, 2006; *Melosh*, 1989]. Detailed counts of blocks around small fresh lunar craters [*Moore et al.*, 1969] show a decrease in the cumulative number and area covered by blocks with increasing distance from the crater rim. The rockiest areas are near the rim where total rock coverage of 40% or higher occur and there is a general decrease in total rock abundance from the rim (from 30% at 1.5 times the radius to 20% at 2 times the radius to 15% and the ambient beyond) [*Bernard and Golombek*, 2001]. In addition, the shape
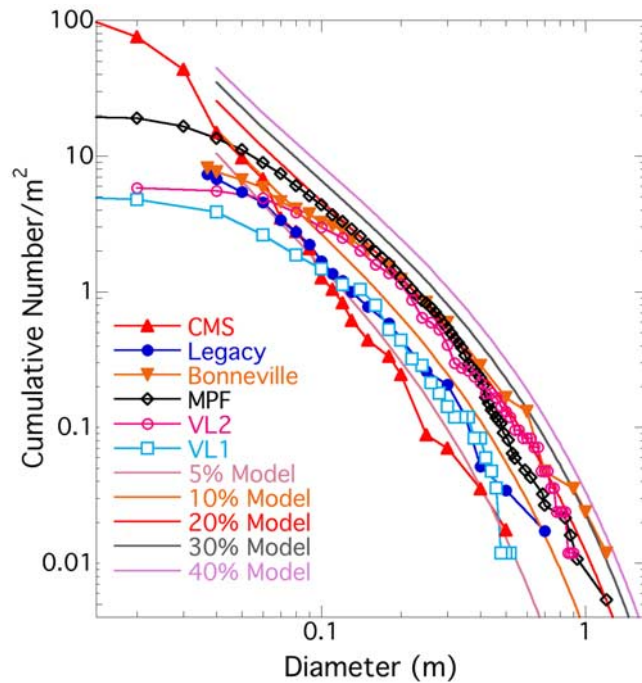
Figure 22. Cumulative number of rocks per meter squared larger than a given diameter versus diameter plots of rocks counted in portions of the CMS, Legacy, and Bonneville panoramas; VL and MPF landing sites and model distributions are based on VL sites, and a rocky location on Earth [*Golombek and Rapp*, 1997; *Golombek et al.*, 2003b] is shown for reference. See text for discussion.

of the size-frequency distribution of ejected blocks is similar to the exponential model distributions developed from Viking data. The measured size-frequency distributions of rocks at the 3 locations are thus consistent with expectations for fresh craters with 35% rock abundance at the rim, decreasing to roughly the ambient at the Legacy panorama site, which is at the edge of the continuous ejecta blanket (>2 times the crater radius). As a result, the rock abundance and maximum block size measured on the ejecta blanket are consistent with expectations for fresh craters on the Moon and further argue that Bonneville is a fresh, relatively unmodified crater on Mars (section 4.1).

[55] The cumulative number versus diameter plots (Figure 22) further illustrates the greater number of pebbles at locations with less dust (and lower albedo [*Golombek et al.*, 2005a]). The cumulative number versus diameter data for the larger rocks at the CMS, Legacy and Bonneville sites generally follow the model distributions for total rock abundances of 5%, 7% and 30%, respectively (see *Golombek et al.* [2003b] for derivation of the model curves in terms of cumulative number). At smaller rock diameters at the Legacy and Bonneville sites the cumulative number of rocks decreases more rapidly than the model distributions similar to the VL and MPF distributions. At CMS the number of pebbles continues to increase and exceeds 100/m^2 for 1 cm pebbles, thereby exceeding the previous maximum of 20/m^2 at MPF. The number of pebbles at these locations correlates directly with the amount of dust inferred from the albedo at these locations [*Golombek et al.*, 2005a],

with higher-albedo locations (VL1, VL2, Legacy and Bonneville) all having fewer pebbles (with total number of rocks >1 cm of <10/m^2), with the low-albedo location (CMS) having the greatest number of pebbles, and with MPF intermediate. Calculations of aerodyamic roughness based on the rock distributions measured at these three sites shows a difference of three orders of magnitude and confirms that it is much more difficult for wind to pick up and move eolian materials from surfaces with greater rock abundance [*Greeley et al.*, 2005a].

5.3.2. Discussion: Sorting and Relation to Thermal Inertia

[56] Results from the Navcam and Pancam clast counts show that clasts are largest and most poorly sorted within areas of higher thermal inertia (Bonneville ejecta and the base of the Columbia Hills). Clast shapes varied little over the entire course of the traverse and are subangular to subrounded [*Crumpler et al.*, 2005]. Clast size distributions indicate a relatively uniform distribution of clasts smaller than 40 cm and clasts larger than 10 to 15 cm are uncommon. The cumulative fractional area versus diameter and cumulative number versus diameter plots of a representative sample of the clast counts of ejecta, crater rim, and high and low-thermal-inertia surfaces are shown in Figures 23 and 24, respectively. The cumulative fractional area plots (Figure 23) show the characteristic exponential decrease in fractional area covered by the larger clasts in these surveys.
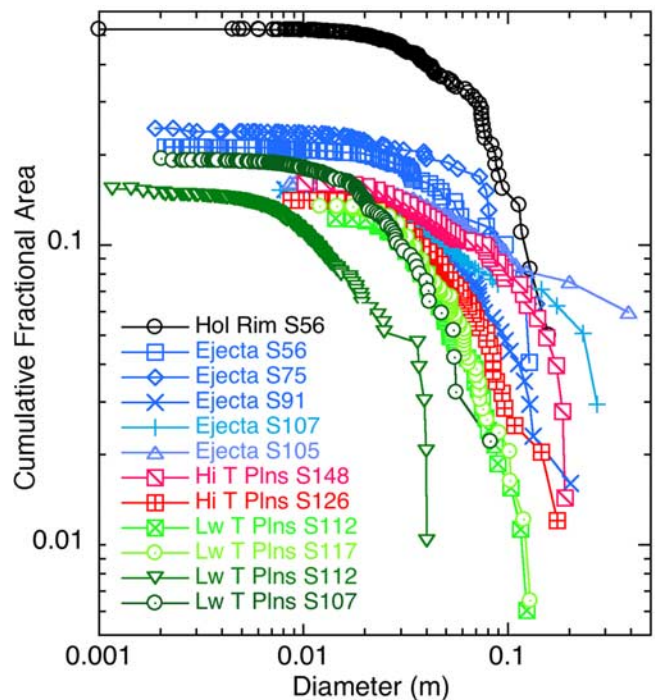
Figure 23. Cumulative fractional area versus diameter plots of rocks counted in clast survey Pancam and Navcam images acquired in different terrains along the rover traverse. Ejecta and hollow rims (blue and black) generally have more area covered by rocks and a less abrupt dropoff in larger diameter clasts than high-thermal-inertia plains (red) and low-thermal-inertia plains (green). Rock count data in Table 2.
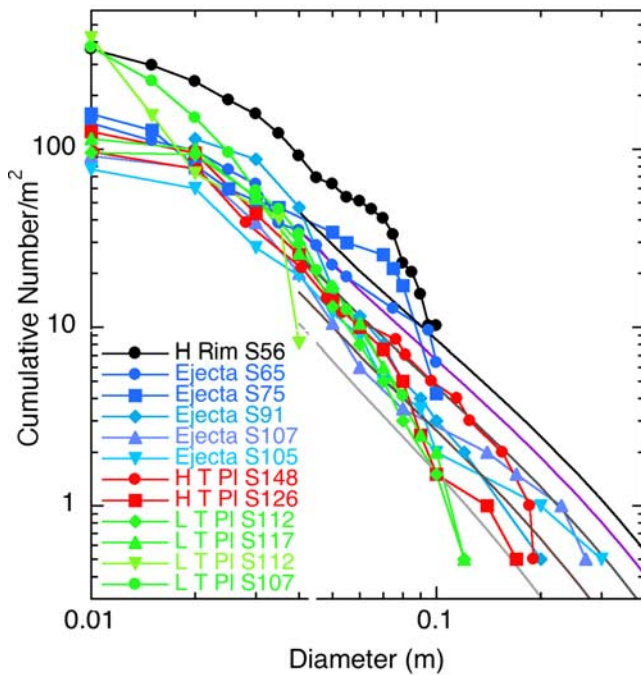
Figure 24. Cumulative number of rocks per meter squared larger than a given diameter versus diameter plot of rocks counted in clast survey Pancam and Navcam images acquired in different terrains along the rover traverse. Model distributions based on Viking Lander sites and rocky locations on Earth [*Golombek and Rapp*, 1997; *Golombek et al.*, 2003b] for 5%, 10%, 20%, 30%, and 40% total rock abundance (lowest to highest solid lines), shown for reference. Ejecta and hollow rim (blue and black) and high-thermal-inertia plains (red) have more large clasts than low-thermal-inertia plains (green) but fewer smaller clasts or pebbles consistent with winnowing of fines on the plains. Rock count data in Table 2.

[57] Higher-thermal-inertia areas show more larger rocks and more area covered by larger rocks, which yields a flatter cumulative area versus diameter clast curve than areas of lower thermal inertia that have far fewer large rocks and a much more abrupt drop off in cumulative area versus diameter [*Moersch et al.*, 2005]. This is demonstrated by inspection of the average $q(k)$ that controls how abruptly the area covered by rocks decreases with increasing diameter [*Golombek and Rapp*, 1997]. For the plotted examples, the average $q(k)$ (absolute value) of the ejecta is 9.4, compared with 13.2 for the high-inertia plains, and 32.1 for the low-inertia plains (Table 2), which are consistent with those of *Moersch et al.* [2005]. The total area covered by clasts in these surveys varies from 10% to 50%, consistent with the clast rich areas surveyed, and is higher in the ejecta (average 24%) than in the plains (average 15%). These results are generally consistent with the rock counts over larger areas when accounting for the small sampling areas and few large rocks.

[58] A similar variation in the rock size-frequency distribution with increasing distance from the Bonneville rim has been observed [*Crumpler et al.*, 2005]. Further, where large rocks (diameter > 10 cm) are common, small rocks (diameter < 10 cm) are less common, and the corresponding

distribution curves are flatter suggesting dust is trapped in areas of large blocks and bury small clasts. Similar distributions in the plains reflect areas where large blocks or their absence appear to modulate dust deposition. Clast abundances on the lee side of large craters and the bottoms of hollows are uniformly low [*Crumpler et al.*, 2005] (Figure 12).

[59] The cumulative number versus diameter plots (Figure 24) show trends consistent with the model distributions with $1-10/m^2$ cumulative number of pebbles greater than 10 cm diameter. In general there are fewer large clasts in low-thermal-inertia plains, with increasing numbers for high-thermal-inertia plains and ejecta. As observed for the larger rock surveys, the total number of small pebbles 1 cm or greater in diameter is greatest (some exceeding $400/m^2$) in the low-thermal-inertia surfaces.

[60] The observed size-frequency distribution of small pebbles as well as nearest neighbor spacing shows that pebbles in the intercrater plains are smaller, better sorted and more evenly spaced than those found near crater rims [*Ward et al.*, 2005]. In contrast, the population of clasts on the ejecta deposits near the rim of Bonneville are dominated by larger, poorly sorted and randomly dispersed clasts. The even spacing of the clasts in the intercrater plains could result from wind turbulence and eddies that produce motion of pebbles from wind drag or saltation induced traction during rare high-wind events during a period of higher atmospheric density [*Ward et al.*, 2005].

6. Eolian Features

[61] A wide variety of wind-related (eolian) features are seen on the floor of Gusev crater [*Greeley et al.*, 2004, 2006]. These include soils deposited under the influence of

Table 2. Representative Navcam and Pancam Clast Survey Count Data

Site[a]	Area, m²	N	CFA	q(k)	k	R
		Ejecta				
W56	0.39	512	0.523	13.11	0.64	0.97
W65	0.31	175	0.212	9.83	0.23	0.97
W75	0.23	419	0.245	9.02	0.26	0.96
C091	2.0	228	0.153	13.94	0.192	0.99
C107	2.0	183	0.159	6.71	0.152	0.94
C105	2.0	154	0.162	3.89	0.163	0.94
		High-Inertia Plains				
C148	2.0	192	0.160	9.67	0.186	0.99
C126	2.0	251	0.141	16.67	0.183	0.99
		Low-Inertia Plains				
C112	2.0	191	0.122	26.82	0.223	0.98
C117	2.0	229	0.135	24.92	0.222	0.98
W112	0.12	573	0.153	49.31	0.177	0.98
W107	0.24	390	0.194	27.43	0.231	0.97
		Hollow Rim				
C60	2.0	203	0.1	0.134	0.118	0.99
		Hollow Interior				
C60	14.5	173	0.03	0.220	0.070	0.96

[a]W and C indicate rock counts from *Ward et al.* [2005] or *Crumpler et al.* [2005], respectively, where the number refers to the rover location or sol where the image was acquired, N is number of rocks, $q(k)$ and k are defined in the text, and CFA is the cumulative fractional area covered by all measured rocks.
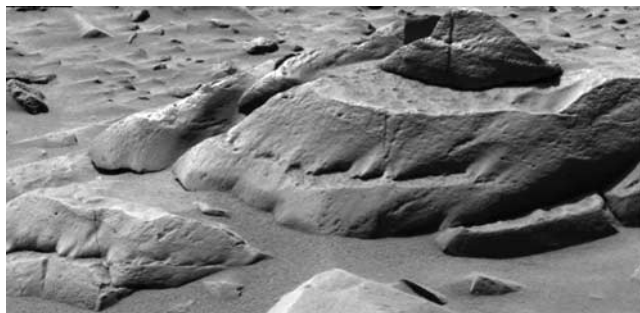
Figure 25. Rocks showing ventifacts at common horizon about 8 cm above their bases indicating burial when eroded by saltating sand and later exhumation. Pancam image 2P131954281SFL1300P2531L7M1 of Terrace rock.

wind, such as dust, bed forms (most of which appear to be ripples formed by saltation induced creep of granules) (Figure 20), and "drifts" of material found in association with rocks, called wind tails (Figure 4b). Wind erosion is indicated by planar surfaces (facets) and grooves (ventifacts) cut into rocks (Figure 25).

[62] Most of soils seen at the CMS and along the traverse to the Columbia Hills are thought to have been emplaced by the wind [*Greeley et al.*, 2004, 2006] (Figure 4). These include the pervasive bright red dust that coats the tops of most rocks and other soils. Dust grains are estimated to be about 3 microns in diameter [*Lemmon et al.*, 2004], and probably settled from the atmosphere. Soils in the ripples and other bed forms consist of dust and coarse sand (several hundred microns in diameter), and often include a surface mono-layer of very coarse sands and granules, 1–4 mm in diameter [*Herkenhoff et al.*, 2004]. The surface monolayer is most likely a lag deposit formed by the removal of smaller grains by the wind. Similarly, lithic fragments as large as 9 mm across are seen in some soil deposits; these are considered to be fragments weathered from local rocks, and to have been rounded by impacts of windblown sand. Soils disturbed by the rover wheels appear relatively darker than undisturbed soils and are basaltic and similar spectrally and compositionally to soils elsewhere on Mars suggesting they are part of a global unit or have been derived from a similar protolith [*Yen et al.*, 2005]. The interior of bed forms "cut" by the rover wheels display a mixture of sand and dust, suggesting that dust has settled on the bed form and then infiltrated downward between the sand grains. On Earth, the presence of infiltrated dust is an indication that the bed form is not currently active because the process of saltation induced creep that forms the bed form normally purges the finer grained dust from the deposit [*Greeley et al.*, 2005b, 2006]. This suggests that most of the bed forms along the traverse are inactive.

[63] Spirit landed in a relatively dark linear feature, inferred to be the track of a dust devil [*Bell et al.*, 2004]. Examination of images taken from orbit before and just after the landing show that the dark streak is a recently formed feature. Microscopic Imager (MI) images of the sands within the streak are relatively free of dust, whereas those outside the streak appear "dusty" [*Herkenhoff et al.*, 2004]. This result confirms the hypothesis that some dark streaks result from the removal of very small amounts of dust to expose a

relatively darker substrate [*Greeley et al.*, 2004, 2006]. The reason that crater rims generally appear brighter in MOC images is likely because the rims are rockier locations with higher aerodynamic roughness, making it difficult for the wind to pick up and move eolian material and in particular dust that has settled from the atmosphere. Conversely, areas with fewer large rocks and lower rock abundance have much lower aerodynamic roughness making it easier for wind to move dust that has settled from the atmosphere. This potentially explains the darker interior of most craters and hollows observed in MOC images.

[64] Many of the rocks observed by Spirit have flat faces or facets and/or grooves cut into their surfaces (Figure 25), giving them the appearance of wind-abraded rocks, or ventifacts, that have been abraded by saltating sand [*Greeley et al.*, 2004, 2006]. Most of the facets and grooves are on the northwest sides of the rocks, and although they are similar in morphology to those seen on rocks at MPF, they are less common at the *Spirit* site. Some of the rocks have adjacent triangular-shaped deposits of soil termed "wind tails" (Figure 4b) that are similar to those seen at previous landing sites on Mars. The size of the wind tails tend to scale with the size of the rock they are adjacent to and the orientation of the tapered part of the wind tail is considered to "point" in the downwind direction. The dark, apparently coarser grained surface of the wind tails suggests they are remnants of formerly more extensive deposits [*Greeley et al.*, 2006].

[65] Bed forms, wind tails, and ventifact facets and grooves indicate the prevailing wind directions at the time of their formation [*Greeley et al.*, 2004, 2006]. Azimuths of some 1500 features analyzed along the traverse suggest that the prevailing formative winds were from the north northwest, a direction that is consistent with afternoon winds predicted by atmospheric models [*Greeley et al.*, 2005b, 2006]. However, most of the bed forms are only moderately asymmetric, suggesting that "reversing" winds are also present. Such winds are predicted to occur at night, when air flow is into the crater from the surrounding high-standing areas, including the Gusev crater rim [*Greeley et al.*, 2005b, 2006].

[66] Many of the rocks display a two-toned appearance with a lighter patination along their base, suggesting that they were partly buried by soils that have subsequently been removed (Figure 26) [*Greeley et al.*, 2004]. Some rocks appear to be "perched" on other rocks, suggesting that they were "lowered" into place by the removal of soils (Figure 26). Many ventifacts originate from a common horizon elevated above the soil (Figure 25), suggesting that the lower part of the rock was shielded by a soil layer that has since eroded away. Some rocks appear undercut in which soil has been removed from their bases. The interpretation of wind tails as a remnant of formerly more extensive deposit also supports the removal of eolian material at the site. These observations suggest that the local surface has been lowered by wind deflation [*Grant et al.*, 2004; *Greeley et al.*, 2004]. Measurements to the heights above the surface for the light toned horizon and the height of the "perched" rocks would indicate localized deflation of 5 cm to as much as 27 cm in some areas [*Greeley et al.*, 2006]. No evidence for repeated burial and exhumation of the surface (e.g., multiple ventifact horizons) has been seen.

Figure 26. Pancam false color composite image showing rocky surface and dusty drift on plains (Columbia Hills in the near background; wall of Gusev visible in the far background ∼80 km distant). This exaggerated color composite emphasizes the two-toned patination of rocks, with darker tops and redder soil-covered bases and perched rocks. Both support deflation of the surface. False color RGB composite generated from images at 750, 530, and 480 nm.

[67] The discovery of active dust devils on the floor of Gusev crater clearly demonstrates that eolian processes are taking place in the current environment. Although the bed forms containing the infiltrated dust indicates that these sands are inactive, the observation of sand grain accumulation on the rover deck on sol 431 [*Greeley et al.*, 2006] could mean that some sand experiences active saltation in the Columbia Hills currently. Present-day winds are also indicated by the asymmetric pattern of abraded material from rocks that were ground by the rover [*Greeley et al.*, 2004].

7. Surficial Geology

[68] Spirit's investigation of the cratered plains in Gusev reveals a surface that is dominated by impact and eolian processes [*Grant et al.*, 2004]. The rocks are uniformly olivine basalts, with variable thin coatings of dust and weathering rinds [*McSween et al.*, 2004; *Christensen et al.*, 2004a; *Bell et al.*, 2004]. Rocks are angular, consistent with expected impact ejecta around craters. There is no evidence for rounded to subrounded boulders, imbricated rocks, or troughs consistent with fluvial processes, which is in marked contrast to their identification at the Mars Pathfinder landing site [*Golombek et al.*, 1997]. Furthermore, counter to interpretations of previous landing sites, there is evidence that the intercrater plains traversed by Spirit inherited some characteristics from an original lava flow surface such as the presence of angular vesicular clasts,

rocks with vesicular layers, delicate scoriaceous clasts, and large blocks of basalt excavated from the larger impact craters. The observed relief of the plains and mapped relations are also comparable to those of terrestrial lava flows, including possible inflation plateaus and the superposition of local relief from multiple flow units onto a regional gradient.

[69] Although we cannot rule out that some of the materials sampled by Spirit are not basaltic debris deposited by fluvial processes, there is no direct evidence gathered by Spirit supporting this interpretation [*Squyres et al.*, 2004]. If the basalts in the cratered plains were delivered by large impacts outside of Gusev or alluvial transport from the highlands down Ma'adim Vallis, they would be expected to sample a range of terrains and have variable mineralogy and chemistry [*Grant et al.*, 2004]. In addition, the size, poor sorting, and lack of rounding of the largest rocks makes their arrival as alluvium from Ma'adim Vallis unlikely. Transporting >1 m diameter rocks tens of kilometers to the landing site by clear water or hyperconcentrated flows is not supported by estimated discharge [*Irwin et al.*, 2004] and derived flow velocity [*Komatsu and Baker*, 1997] for Ma'adim Vallis [*Grant et al.*, 2004] or by the absence of obvious flood features on the cratered plains. Finally, it is unlikely that the numerous rocks larger than 1 to 2 m could be emplaced as ejecta from outside of Gusev, because they would be unlikely to survive ballistic sedimentation over large distances [*Melosh*, 1989].

[70] Spirit's investigation of Bonneville crater indicates that more than the upper 10 m of the cratered plains is an impact-generated regolith that likely formed in basalt lava flows. No bedrock is apparent in the walls, and rocks exposed in the walls (including the largest ∼2.5 m in diameter) appear jumbled (Figure 19b). Even where small craters impacted into the wall of Bonneville, no bedrock is exposed. The low wall slopes of the crater indicate that slumping during the final stages of crater formation was not impeded by bedrock [*Grant et al.*, 2004]. The largest rocks (∼2.5 m) are found around the largest craters and appear to reflect impact transport during crater formation [*Melosh*, 1989] of more intact preexisting materials (likely intact basalt flows with widely spaced cooling joints). Finally, the sharp contrast between Bonneville's ejecta deposits and surfaces beyond the ejecta (e.g., surrounding the lander), indicate that surfaces of the crater facies remain relatively pristine and are not mantled by significant thicknesses of younger fine grained debris and such materials are not observed on the eastern crater walls. These arguments suggest that the crater formed largely in loose rubble, but that the largest observed ejecta blocks may be derived from locally more competent rocks below the crater (e.g., lava flows).

[71] As a result, a volcanic origin for the cratered plains is favored. Although no obvious fissures or other volcanoes are visible on the floor of Gusev crater, plains to the northeast have been interpreted as volcanic [*Milam et al.*, 2003]. The sources of the lava flows that cover most of the floor of Gusev may have been from fissure style eruptions similar to lunar mare basalts [*Greeley et al.*, 2005a] that have been covered by subsequent lava flows or are no longer preserved due to subsequent impacts. While lacustrine deposits are plausibly present beneath the volcanic cover, it is clear now that the interior deposits of Gusev

crater are not entirely lacustrine in origin. Furthermore, if the interpretation of the young rumpled flow emanating from Ma'adim Valis as a debris flow is correct (Figure 1), it would suggest that there have been alternating episodes of water deposited materials interspersed with volcanic basalt infilling as among the most recent geologic events in Gusev crater.

8. Discussion: Climate Implications

[72] Spirit's observations of the surficial geology of the cratered plains indicate that impacts produced a rubble layer over 10 m thick and eolian activity filled in the craters to produce hollows, leaving behind rocky ejecta, a pebble-rich desert pavement, and presently inactive eolian bed forms that represent a lag. In this interpretation, excavation during impact deposited ejecta with widely varying grain sizes and fractured rocks, which was in disequilibrium with the eolian regime [Grant et al., 2004; Greeley et al., 2004, 2006]. This would lead to deflation of ejected fines, exposing fractured rocks, and creating a population of perched coarser fragments. Transported fines would be trapped within the depressions (craters) creating the hollows. Trenching in Laguna hollow near the edge of the Bonneville ejecta exposed unaltered basaltic fines capped by a thin layer of brighter, finer, globally pervasive dust [Arvidson et al., 2004]. The dust-free nature of sediment in the hollows coupled with their uniformly filled appearance implies relatively rapid modification of locally derived sediment to their current more stable form. As sand supply that could be moved by the wind decreased due to deposition in craters, little further activity occurred leaving the inactive bed forms and sediment-filled hollows.

[73] The observed exhumation and deflation of the cratered plains surface traversed by Spirit represents the cumulative change of the surface since the Hesperian, or ~3.0 Ga [Hartmann and Neukum, 2001], which provides a clue to the climate over this time [Golombek et al., 2005b]. The gradation and deflation of ejected fines of ~5–25 cm and deposition in craters to form hollows provides an estimate of the average rate of erosion or redistribution via the vertical removal of material per unit time typically measured on Earth in Bubnoff units (1 B = 1 μ/yr) [Judson and Ritter, 1964; Saunders and Young, 1983]. The deflation and exhumation of rocks at Gusev suggest of order 10 cm average deflation or redistribution at the site. Over the age of the cratered plains (Late Hesperian/Early Amazonian or 3 Ga) this argues for extremely slow average erosion rates of ~0.03 nm/yr or between 0.02 nm/yr and 0.08 nm/yr. Rates of redistribution this slow argue that little has happened at the site except periodically high deflation (following impacts) of locally derived surface fines to fill the impact craters.

[74] Such erosion rates fall between those estimated in a similar manner at the Mars Pathfinder landing site (~0.01 nm/yr) [Golombek and Bridges, 2000] and at the Viking Lander 1 site (~1 nm/yr) [Arvidson et al., 1979] and argue for very little net change of these surfaces implying that a dry and desiccating environment similar to today's has been active throughout the Hesperian and Amazonian [Golombek and Bridges, 2000] or since ~3.7 Ga. These rates likely represent redistribution or localized deflation

rather than true erosion or denudation, although they can be compared to average erosion rates as a coarse indicator of the climatic conditions active over the Amazonian. In reality, the redistribution of sand probably occurred relatively rapidly (at a higher rate over a short period), but then no further erosion occurred, yielding the extremely slow calculated long-term rates [Golombek and Bridges, 2000]. This is in contrast to the redistribution or cycling of dust from the atmosphere to the surface and then back into the atmosphere which is occurring at high rates (and leaving little trace on the surface). Mars Pathfinder and the Mars Exploration Rovers (for the first 3 months) measured a decrease in solar cell output of 0.29% per sol, which translates to a deposition rate of order 10 micron/yr [Landis and Jenkins, 2000; Arvidson et al., 2004; Lemmon et al., 2004] for the observed dust particle size [Tomasko et al., 1999; Lemmon et al., 2004]. This would result in meters thick accumulations of dust within a comparatively short span of a million years. Because such accumulations are not observed at any of the landing sites, dust must be removed as rapidly as it is being deposited over relatively short time scales. Frequent dust devils observed at the Mars Pathfinder and Spirit landing sites clearly play a role in the removal of dust from these surfaces.

[75] Long-term average erosion rates during the Amazonian from deflation and filling of craters in the Gusev plains are so low that they indicate a dry and desiccating climate similar to today's for the past 3 Ga [Golombek et al., 2005b]. An environment in which liquid water is not stable is also in accord with the lack of chemical weathering indicated by exposures of basalt and olivine basalt at Gusev [McSween et al., 2004, 2006] and throughout equatorial Mars [Hoefen et al., 2003; Christensen et al., 2003] and in the soils of Gusev and Meridiani [Yen et al., 2005; Christensen et al., 2004a, 2004b] and the observed pattern of crater gradation at Gusev [Grant et al., 2006], which shows no evidence for erosion by liquid water.

9. Conclusions

[76] 1. Spirit's investigation of the cratered plains in Gusev crater reveals a surface dominated by impact and to a lesser extent, eolian processes in concert with the dominant features observed in high-resolution images from orbit. The surfaces explored are generally low-relief rocky plains dominated by shallow soil-filled circular depressions, typically with rocky rims, called hollows. Rocks are dark, fine-grained basalts that are angular, consistent with impact ejecta around craters. There is no evidence for rounded to subrounded boulders, imbricated rocks, or troughs that would argue for fluvial processes as expected from the morphologic setting inside Gusev crater or the possible young debris flow that emanates from Ma'adim Vallis revealed in THEMIS images that covers the western part of the landing ellipse.

[77] 2. Spirit's investigation of Bonneville crater indicates that the upper 10 m of the cratered plains is an impact generated regolith that likely formed in basalt lava flows. The largest rocks observed are in ejecta near the rims of the largest craters, suggesting they were excavated from relatively intact basalt flows at depth. No outcrop has been seen anywhere in the craters or cratered plains.

[78] 3. Systematic field observations across Spirit's traverse correspond to terrains mapped in MOC images. Vesicular clasts and delicate scoria similar to original lava flow tops have been found on low-thermal-inertia intercrater plains just east of Missoula crater ejecta. Spirit traversed "tabled terrain" (rough, generally higher-thermal-inertia terrain characterized by local elongate plateaus or tables) to the south, "whaleback terrain" (widely dispersed hummocks or whale-back-shaped swells) to the north, and transitional terrain in between. A south to north topographic gradient of up to several degrees is apparent in Navcam panoramas and MOLA topography, consistent with an original lava flow surface emplaced from the south. The tabled terrain is consistent with an upper inflated surface of lava flows with adjacent collapse depressions that typically occur where the underlying surface gradient decreases and where basalt flows encounter obstacles (Columbia Hills).

[79] 4. Hollows, tens of centimeters to tens of meters in diameter, show a range of preservation states consistent with old and small craters being filled in with sediment and nearby ejecta with time. Some are shallow circular depressions with slightly lower rock abundance without rocky rims. Others are relatively fresh with rocky rims, rocky ejecta and more relief. An increase in rock abundance of only 7% from subsequent crater ejecta would make a 5 m diameter hollow difficult to identify from the background plains.

[80] 5. The size frequency distribution of 58 hollows, 1–10 m in diameter mapped along the rover traverse during the first 90 sols exhibits a power law −1.5 slope and forms a continuum with craters 10 m to 600 m in diameter mapped in MOC images that fit a power law with −2 slope. This distribution along with their morphology (circular depressions with rocky rims) strongly argues that hollows are impact craters. The slightly lower power law slope of the hollows is likely produced by the preferential loss of smaller hollows due to resurfacing or erosion. The hollows observed by Spirit represent the first statistical sample of impact craters on Mars at meter to submeter diameter scale.

[81] 6. Craters larger than ~100 m diameter show a progression in degradation state from Bonneville (210 m diameter), with fresh ejecta, raised rim, and little fill; to Lahontan (90 m diameter), with less fresh ejecta, more fill, and lower wall slopes; to Missoula (163 m diameter), with less fresh ejecta, more fill, and low wall slopes; to Searles crater west of Lahontan (~100 m in diameter), which possesses only 1–2 m of relief, and is mainly filled by a mix of eolian sediments and ejecta blocks. The observed gradation sequence mostly involves the filling of craters with sediment and younger ejecta and there is no evidence for the characteristic pattern of crater erosion dominated by water that occurs on Earth.

[82] 7. Crater morphometry and degradation state argue that most or all of the craters and hollows are secondaries rather than primaries. The poorly circular planforms, low depth-to-diameter ratios (<0.1) and wall gradients for the Gusev craters are more consistent with fairly pristine secondary craters formed into unconsolidated rubble rather than primaries (which are twice as deep at formation) that have been heavily modified. Bonneville, the freshest large crater needs only a few meters of fill to account for the observed depth/diameter (d/D) ratio if it formed as a relatively pristine secondary. The d/D ratio of the freshest, deepest hollows is also close to that expected for secondaries, with more degraded and filled hollows having lower d/D ratios. The morphometry and form of the freshest small craters superposed on Bonneville (the freshest large crater) observed by Spirit also argues that they are secondaries with low d/D ratios, triplet clusters, and noncircular planforms.

[83] 8. The size-frequency distribution of rocks >0.1 m diameter measured in >70° sectors at Columbia Memorial Station (low-inertia plains), Legacy (edge of continuous ejecta), and Bonneville crater rim panoramas out to 10 m distance generally follows the exponential model distribution based on Viking Lander and rocky locations on Earth used in landing site selection work for total rock abundances of 5%, 7% and 35% at the three respective sites. The rock distribution at CMS displays power law behavior from 0.1 to 0.03 m diameter with a total of about 11% of the surface covered by rocks at this site (about half is covered by pebbles, making this the most pebble rich landing site yet visited on Mars). The rock abundance increases as the thermal inertia increases at the three sites.

[84] 9. Regular clast surveys in Navcam and Pancam images along the traverse also show a positive relationship between thermal inertia and total rock abundance and the exponential factor that controls how steeply the area covered by rocks decreases with increasing size. Higher-thermal-inertia areas generally show more larger rocks and more area covered by larger rocks, which yields a flatter cumulative area versus diameter curve than areas of lower thermal inertia that have far fewer large rocks and a much more abrupt drop off in cumulative area versus diameter. Lower-thermal-inertia areas with lower overall rock abundance have more pebbles that are better sorted and more evenly spaced than higher-thermal-inertia locations with more, larger rocks. This argues that the pebble rich surface in the low-thermal-inertia plains is similar to a desert pavement or lag produced by deflation of fines, with wind drag or saltation induced traction on the pebbles producing their even spacing and sorting. Conversely, rocky ejecta deposits and high-thermal-inertia plains tend to be dustier with higher aerodynamic roughness making it more difficult for the wind to effectively move eolian materials. This process provides a ready explanation for the widespread bright (dusty) rims of craters and their darker, less dusty interiors observed in MOC images.

[85] 10. Eolian features identified by the Spirit rover include bed forms (mostly ripples), "drifts" of material found in association with rocks, called wind tails, and planar surfaces (facets) and grooves (ventifacts) cut into rocks by impacts of saltating sand. Ripples investigated have surfaces with a monolayer of coarse-grained sand and granules covered with dust and more poorly sorted, but generally finer grained interiors. The granule rich surface and dust cover suggest a lag deposit with saltation induced creep no longer occurring.

[86] 11. The Spirit observations are consistent with the formation of the cratered plains by a process in which excavation during impact deposits ejecta with widely varying grain sizes and fractured rocks that was in disequilibrium with the eolian regime. Deflation of ejected fines exposed the fractured rocks, and created a population of perched coarser fragments. Transported fines would be

rapidly trapped within the depressions (craters) creating the hollows, which would reduce the sand supply and lead to a surface that was in equilibrium with the eolian regime and thus generally inactive (except for dust cycling).

[87] 12. Deflation of the surface by ~5 to 25 cm is suggested by two-toned rocks with a redder patination along their bases, ventifacts that originate from a common horizon above the soil (suggesting that the lower part of the rock was shielded), rocks that appear to be perched on top of other rocks, and some undercut rocks, in which the soil has been removed from their bases. The observed deflation of the surface thus represents the cumulative change of the surface since the Hesperian, or ~3.0 Ga, which provides a clue to the climate over this time. Extremely slow average erosion rates of ~0.03 nm/yr (between 0.02 nm/yr and 0.08 nm/yr) for the cratered plains are generally comparable to those estimated in a similar manner at the Mars Pathfinder and Viking 1 landing sites and argue for very little long-term net change of the surface implying a dry and desiccating environment similar to today's has been active throughout the Hesperian and Amazonian (~3.7 Ga to present).

References

Allen, J. R. L. (1985), *Principles of Physical Sedimentology*, 272 pp., Allen and Unwin, St Leonards, NSW, Australia.

Arvidson, R., E. Guiness, and S. Lee (1979), Differential aeolian redistribution rates on Mars, *Nature*, 278, 533–535.

Arvidson, R. E., et al. (2004), Localization and physical properties experiments conducted by Spirit at Gusev crater, *Science*, 305, 821–824, doi:10.1126/science.1099922.

Arvidson, R. E., et al. (2006), Overview of the Spirit Mars Exploration Rover Mission to Gusev crater: Landing site to Backstay Rock in the Columbia Hills, *J. Geophys. Res.*, 111, E02S01, doi:10.1029/2005JE002499.

Bell, J. F., III, et al. (2004), Pancam multispectral imaging results from the Spirit rover at Gusev crater, *Science*, 305, 800–806.

Bernard, D. E., and M. P. Golombek (2001), Crater and rock hazard modeling for Mars landing, in *American Institute of Aeronautics and Astronautics, Space 2001 Conference, Albuquerque, NM, August 2001* [CD-ROM], pap. AIAA-2001-4697, 17 pp., Am. Inst. of Aeronaut. and Astronaut., Reston, Va.

Brakenridge, G. R. (1990), The origin of fluvial valleys and early geologic history, Aeolis Quadrangle, Mars, *J. Geophys. Res.*, 95, 17,289–17,308.

Brown, W. K., and K. H. Wohletz (1995), Derivation of the Weibull distribution based on physical principles and its connection to the Rosin-Rammler and lognormal distributions, *J. Appl. Phys.*, 78, 2758–2763.

Cabrol, N. A., E. A. Grin, and G. Dawidowicz (1996), Ma'adim Vallis revisited through new topographic data: Evidence for an ancient intervalley lake, *Icarus*, 123, 269–283.

Cabrol, N. A., E. A. Grin, and R. Landheim (1998), Ma'adim Vallis evolution: Geometry and models of discharge rate, *Icarus*, 132, 362–377.

Cabrol, N. A., et al. (2003), Exploring Gusev crater with Spirit: Review of science objectives and testable hypotheses, *J. Geophys. Res.*, 108(E12), 8076, doi:10.1029/2002JE002026.

Carr, M. H., and G. D. Clow (1981), Martian channels and valleys: Their characteristics, distribution and age, *Icarus*, 48, 91–117.

Castaño, R., M. Judd, T. Estlin, R. Anderson, L. Scharenbroich, L. Song, D. Gaines, F. Fisher, D. Mazzoni, and A. Castaño (2004), Autonomous onboard traverse science system, paper 1375 presented at the *Aerospace Conference*, Inst. of Electr. and Electr. Eng., Big Sky, Mont., March.

Christensen, P. R. (1986), The spatial distribution of rocks on Mars, *Icarus*, 68, 217–238.

Christensen, P. R., et al. (2003), Morphology and composition of the surface of Mars: Mars Odyssey THEMIS results, *Science*, 300, 2056–2061.

Christensen, P. R., et al. (2004a), Initial results from the Miniature Thermal Emission Spectrometer experiment at the Spirit landing site at Gusev crater, *Science*, 305, 837–842.

Christensen, P. R., et al. (2004b), Mineralogy at Meridiani Planum from the Mini-TES experiment on the Opportunity rover, *Science*, 306, 1733–1739.

Christensen, P. R., et al. (2005), Mars Exploration Rover candidate landings sites as viewed by THEMIS, *Icarus*, 176, 12–43, doi:10.1016/j.icarus.2005.01.004.

Crumpler, L. S., et al. (2005), Mars Exploration Rover geologic traverse by the Spirit rover in the plains of Gusev crater, Mars, *Geology*, 33(10), 809–812, doi:10.1130/G21673.1.

Fergason, R. L., and P. R. Christensen (2003), Thermal inertia using THEMIS infrared data, *Proc. Lunar Planet. Sci. Conf. 34th*, abstract 1785.

Fergason, R. L., P. R. Christensen, J. F. Bell III, M. P. Golombek, K. Herkenhoff, H. H. Kieffer, and R. Sullivan (2006), The physical properties of the Mars Exploration Rover landing sites as inferred from Mini-TES derived thermal inertia, *J. Geophys. Res.*, doi:10.1029/2005JE002583, in press.

Garvin, J. P., S. E. H. Sakimoto, and J. J. Frawley (2003), Craters on Mars: Global geometric properties from gridded MOLA topography, in *Sixth International Conference on Mars, July 20–25, 2003, Pasadena, CA* [CD-ROM], abstr. 3277, Lunar and Planet. Inst., Houston, Tex.

Gilvarry, J. J. (1961), Fracture of brittle solids I. Distribution function for fragment size in single fracture (theoretical), *J. Appl. Phys.*, 32, 391–399.

Gilvarry, J. J., and B. H. Bergstrom (1961), Fracture of brittle solids II. Distribution function for fragment size in single fracture (experimental), *J. Appl. Phys.*, 32, 400–410.

Goldspiel, J. M., and S. W. Squyres (1991), Ancient aqueous sedimentation on Mars, *Icarus*, 89, 392–410.

Golombek, M. P., and N. T. Bridges (2000), Erosion rates on Mars and implications for climate change: Constraints from the Pathfinder landing site, *J. Geophys. Res.*, 105, 1841–1853.

Golombek, M., and D. Rapp (1997), Size-frequency distributions of rocks on Mars and Earth analog sites: Implications for future landed missions, *J. Geophys. Res.*, 102, 4117–4129.

Golombek, M. P., et al. (1997), Overview of the Mars Pathfinder Mission and assessment of landing site predictions, *Science*, 278, 1743–1748.

Golombek, M. P., et al. (2003a), Selection of the Mars Exploration Rover landing sites, *J. Geophys. Res.*, 108(E12), 8072, doi:10.1029/2003JE002074.

Golombek, M. P., A. F. C. Haldemann, N. K. Forsberg-Taylor, E. N. DiMaggio, R. D. Schroeder, B. M. Jakosky, M. T. Mellon, and J. R. Matijevic (2003b), Rock size-frequency distributions on Mars and implications for Mars Exploration Rover landing safety and operations, *J. Geophys. Res.*, 108(E12), 8086, doi:10.1029/2002JE002035.

Golombek, M. P., et al. (2005a), Assessment of Mars Exploration Rover landing site predictions, *Nature*, 436, 44–48, doi:10.1038/nature03600.

Golombek, M. P., J. A. Grant, L. S. Crumpler, R. Greeley, R. E. Arvidson, and the Athena Science Team (2005b), Climate change from the Mars Exploration Rover landing sites: From wet in the Noachian to dry and desiccating since the Hesperian, *Proc. Lunar Planet. Sci. Conf. 34th*, abstract 1539.

Grant, J. A., et al. (2004), Surficial deposits at Gusev crater along Spirit rover traverses, *Science*, 305, 807–810, doi:10.1126/science.1099849.

Grant, J. A., et al. (2006), Crater gradation in Gusev crater and Meridiani Planum, Mars, *J. Geophys. Res.*, 111, E02S08, doi:10.1029/2005JE002465.

Greeley, R., and D. E. Gault (1979), Endogenic craters on basaltic lava flows: Size-frequency distributions, *Proc. Lunar Planet. Sci. Conf. 10th*, 2919–2933.

Greeley, R., and J. E. Guest (1987), Geologic map of the eastern equatorial region of Mars, *U.S. Geol. Surv. Misc. Geol. Invest. Map*, I-1802-B.

Greeley, R., et al. (2004), Wind-related processes detected by the Spirit rover at Gusev crater, *Science*, 305, 810–813.

Greeley, R., B. H. Foing, H. Y. McSween, G. Neukum, P. Pinet, M. van Kan, S. C. Werner, D. A. Williams, and T. E. Zegers (2005a), Fluid lava flows in Gusev crater, Mars, *J. Geophys. Res.*, 110, E05008, doi:10.1029/2005JE002401.

Greeley, R., et al. (2005b), Martian variable features: New insight from the Mars Express Orbiter and the Mars Exploration Rover Spirit, *J. Geophys. Res.*, 110, E06002, doi:10.1029/2005JE002403.

Greeley, R., et al. (2006), Gusev crater: Wind-related features and processes observed by the Mars Exploration Rover, Spirit, *J. Geophys. Res.*, 111, E02S09, doi:10.1029/2005JE002491.

Grin, E. A., and N. A. Cabrol (1997), Limnologic analysis of Gusev crater paleolake, Mars, *Icarus*, 130, 461–474.

Hartmann, W. K., and G. Neukum (2001), Cratering chronology and the evolution of Mars, *Space Sci. Rev.*, 96, 165–194.

Herkenhoff, K. E., et al. (2004), Textures of the soils and rocks at Gusev crater from Spirit's microscopic imager, *Science*, *305*, 824–826.

Hodges, C. A., and H. J. Moore (1994), Atlas of volcanic landforms on Mars, *U.S. Geol. Surv. Prof. Pap.*, *1534*, 194 pp.

Hoefen, T., R. N. Clark, J. L. Bandfield, M. D. Smith, J. C. Pearl, and P. R. Christensen (2003), Discovery of olivine in the Nili Fossae region of Mars, *Science*, *302*, 627–630.

Hon, K. J., J. Kauahikaua, R. Denlinger, and K. McKay (1994), Emplacement and inflation of pahoehoe flow sheets: Observations and measurements of active flows on Kilauea volcano, Hawaii, *Geol. Soc. Am. Bull.*, *106*, 351–383.

Hurst, M., M. P. Golombek, and R. Kirk (2004), Small crater morphology within Gusev crater and Isidis Planitia: Evidence for widespread secondaries on Mars, *Proc. Lunar Planet. Sci. Conf. 35th*, abstract 2068.

Irwin, P. I., T. A. Maxwell, A. D. Howard, R. A. Craddock, and D. W. Leverington (2002), A large paleolake basin at the head of Ma'adim Vallis, Mars, *Science*, *296*, 2209–2212.

Irwin, R. P., III, A. D. Howard, and T. A. Maxwell (2004), Geomorphology and hydraulics of Ma'adim Vallis, Mars, during a Noachian/Hesperian boundary paleoflood, *Proc. Lunar Planet. Sci. Conf. 35th*, abstract 1852.

Judson, S., and D. F. Ritter (1964), Rates of regional denudation in the United States, *J. Geophys. Res.*, *69*, 3395–3401.

Kirk, R. L., E. Howington-Kraus, B. Redding, D. Galuszka, T. M. Hare, B. A. Archinal, L. A. Soderblom, and J. M. Barrett (2003), High-resolution topomapping of candidate MER landing sites with Mars Orbiter Camera narrow-angle images, *J. Geophys. Res.*, *108*(E12), 8088, doi:10.1029/2003JE002131.

Komar, P. D. (1979), Comparisons of the hydraulics of water flows in Martian outflow channels with flows of similar scale on Earth, *Icarus*, *37*, 156–181.

Komatsu, G., and V. R. Baker (1997), Paleohydrology and flood geomorphology of Ares Vallis, *J. Geophys. Res.*, *102*, 4151–4160.

Kuiper, G. P. (1966), Terrestrial and lunar collapse depressions, *NASA Tech. Rep.*, *32-800*, 51–90.

Kuzmin, R. O., R. Greeley, R. Landheim, N. A. Cabrol, and J. D. Farmer (2000), Geologic map of the MTM-15,182 and MTM-15187 quadrangles, Gusev crater–Ma'adim Vallis region, Mars, *U.S. Geol. Surv. Misc. Geol. Invest. Map*, I-2666.

Landis, G. A., and P. P. Jenkins (2000), Measurement of the settling rate of atmospheric dust on Mars by the MAE instrument on Mars Pathfinder, *J. Geophys. Res.*, *105*, 1855–1857.

Lemmon, M. T., et al. (2004), Atmospheric imaging results from the Mars Exploration Rovers: Spirit and Opportunity, *Science*, *306*, 1753–1756.

Li, R., et al. (2006), Spirit rover localization and topographic mapping at the landing site of Gusev crater, Mars, *J. Geophys. Res.*, *111*, E02S06, doi:10.1029/2005JE002483.

Martínez-Alonso, S., B. M. Jakosky, M. T. Mellon, and N. E. Putzig (2005), A volcanic interpretation of Gusev Crater surface materials from thermophysical, spectral, and morphological evidence, *J. Geophys. Res.*, *110*, E01003, doi:10.1029/2004JE002327.

McCauley, J. F. (1973), Mariner 9, evidence for wind erosion in equatorial and mid-latitude regions of Mars, *J. Geophys. Res.*, *78*, 4123–4138.

McEwen, A. S., B. S. Preblich, E. P. Turtle, N. A. Artemieva, M. P. Golombek, M. Hurst, R. L. Kirk, D. M. Burr, and P. R. Christensen (2005), The rayed crater Zunil and interpretations of small impact craters on Mars, *Icarus*, *176*, 351–381.

McSween, H. Y., et al. (2004), Basaltic rocks analyzed by the Spirit rover in Gusev crater, *Science*, *305*, 842–845.

McSween, H. Y., et al. (2006), Characterization and petrologic interpretation of olivine-rich basalts at Gusev crater, Mars, *J. Geophys. Res.*, *111*, E02S10, doi:10.1029/2005JE002477.

Melosh, H. J. (1989), *Impact Cratering*, 245 pp., Oxford Univ. Press, New York.

Milam, K. A., K. R. Stockstill, J. E. Moersch, H. Y. McSween Jr., L. L. Tornabene, A. Ghosh, M. B. Wyatt, and P. R. Christensen (2003), THEMIS characterization of the MER Gusev crater landing site, *J. Geophys. Res.*, *108*(E12), 8078, doi:10.1029/2002JE002023.

Moersch, J. E., et al. (2005), Comparison of orbital infrared observations and surface measurements by the Mars Exploration Rover Spirit at Gusev crater, *Proc. Lunar Planet. Sci. Conf. 36th*, abstract 2020.

Moore, H. J., R. J. Pike, and G. E. Ulrich (1969), Lunar terrain and traverse data for lunar roving vehicle design study, Prelim. U. S. Geol. Surv. Rep., March 19, 1969, U. S. Geological Survey, 1969.

Mueller, K., and M. Golombek (2004), Compressional structures on Mars, *Annu. Rev. Earth Planet. Sci.*, *32*, 435–464, doi:10.1146/annurev.earth.32.101802.120553.

Norris, J. S., M. W. Powell, M. A. Vona, P. G. Backes, and J. V. Wick (2005), Mars Exploration Rover operations with the Science Activity Planner, *paper 7803-8914 presented at the International Conference on Robotics and Automation*, Inst. Electr. and Electr. Eng., Barcelona, Spain, 18–22 April.

Pike, R. J. (1977), Size-dependence in the shape of fresh impact craters on the moon, in *Impact and Explosion Cratering*, edited by D. J. Roddy and R. B. Merrill, pp. 489–509, Elsevier, New York.

Pike, R. J., and D. E. Wilhelms (1978), Secondary-impact craters on the Moon: Topographic form and geologic process, *Proc. Lunar Planet. Sci. Conf. 9th*, 907–909.

Rice, J. W., Jr., P. R. Christensen, S. W. Ruff, and J. C. Harris (2003), Martian fluvial landforms: A THEMIS perspective after one year at Mars, *Proc. Lunar Planet. Sci. Conf. 34th*, abstract 2091.

Rosin, P., and E. Rammler (1933), The laws governing the fineness of powdered coal, *J. Inst. Fuel*, *7*, 29–36.

Saunders, I., and A. Young (1983), Rates of surface processes on slopes, slope retreat and denudation, *Earth Surf. Processes Landforms*, *8*, 473–501.

Squyres, S. W., et al. (2004), The Spirit rover's Athena science investigation at Gusev crater, Mars, *Science*, *305*, 794–799.

Tanaka, K. L. (1986), The stratigraphy of Mars, *Proc. Lunar Planet. Sci. Conf. 17th*, Part 1, *J. Geophys. Res.*, *91*, suppl., E139–E158.

Tomasko, L., R. Doose, M. Lemmon, P. H. Smith, and E. Wegryn (1999), Properties of dust in the Martian atmosphere from the Imager for Mars Pathfinder, *J. Geophys. Res.*, *104*, 8987–9007.

Walker, G. P. L. (1991), Structure, and origin by injection under surface crust, of tumuli, "lava rises," "lava-rise pits," and "lava inflation clefts" in Hawaii, *Bull. Volcanol.*, *53*, 546–558.

Ward, J. G., R. E. Arvidson, and M. Golombek (2005), The size-frequency and areal distribution of rock clasts at the Spirit landing site, Gusev crater, Mars, *Geophys. Res. Lett.*, *32*, L11203, doi:10.1029/2005GL022705.

Wohletz, K. H., M. F. Sheridan, and W. K. Brown (1989), Particle size distributions and the sequential fragmentation/transport theory applied to volcanic ash, *J. Geophys. Res.*, *94*, 15,703–15,721.

Wood, C. A., and L. Andersson (1978), New morphometric data for fresh lunar craters, *Proc. Lunar Planet Sci. Conf. 9th*, 3669–3689.

Yen, A. S., et al. (2005), An integrated view of the chemistry and mineralogy of Martian soils, *Nature*, *436*, 49–54, doi:10.1038/nature03637.

Zimbelman, J. R., and A. K. Johnston (2001), Improved topography of the Carrizozo lava flow: Implications for emplacement conditions, *N. M. Mus. Nat. Hist. Sci. Bull.*, *18*, 131–136.

————————

R. E. Arvidson and J. G. Ward, Department of Earth and Planetary Sciences, Washington University, St. Louis, MO 63130, USA.

J. F. Bell III and S. W. Squyres, Department of Astronomy, Cornell University, Ithaca, NY 14853, USA.

N. A. Cabrol, NASA Ames Research Center, Moffett Field, CA 94035, USA.

A. Castaño, R. Castaño, M. P. Golombek, A. F. C. Haldemann, and T. J. Parker, Jet Propulsion Laboratory, California Institute of Technology, Pasadena, CA 91109, USA. (mgolombek@jpl.nasa.gov)

P. R. Christensen, R. L. Fergason, R. Greeley, and J. W. Rice Jr., Department of Geological Sciences, Arizona State University, Tempe, AZ 85287, USA.

L. S. Crumpler, New Mexico Museum of Natural History and Science, Albuquerque, NM 87104, USA.

J. A. Grant, Smithsonian Institution, Washington, DC 20560, USA.

R. Li, Department of Civil and Environmental Engineering and Geodetic Science, Ohio State University, Columbus, OH 43210, USA.

J. E. Moersch, Department of Geological Sciences, University of Tennessee, Knoxville, TN 37996, USA.